Lysosome docking to WIPI1 rings and ER-connected phagophores occurs during DNAJB12- and GABARAP-dependent selective autophagy of misfolded P23H-rhodopsin

Andrew Kennedy[a], Hong Yu Ren[a], Victoria J. Madden[b], and Douglas M. Cyr[a,*]
[a]Department of Cell Biology and Physiology, School of Medicine, and [b]Department of Pathology and Laboratory Medicine, University of North Carolina at Chapel Hill, Chapel Hill, NC 27599

ABSTRACT **We report on how the endoplasmic reticulum (ER)-associated-autophagy pathway (ERAA) delivers P23H-rhodopsin (P23H-R) to the lysosome. P23H-R accumulates in an ERAD-resistant conformation that is stabilized in a detergent-soluble state by DNAJB12 and Hsp70. P23H-R, DNAJB12, and FIP200 colocalize in discrete foci that punctuate the rim of omegasome rings coated by WIPI1. Loss of DNAJB12 function prevents the association of P23H-R containing ER tubules with omegasomes. P23H-R tubules thread through the wall of WIPI1 rings into their central cavity. Transfer of P23H-R from ER-connected phagophores to lysosomes requires GABARAP and is associated with the transient docking of lysosomes to WIPI1 rings. After departure from WIPI1 rings, new patches of P23H-R are seen in the membranes of lysosomes. The absence of GABARAP prevents transfer of P23H-R from phagophores to lysosomes without interfering with docking. These data identify lysosome docking to omegasomes as an important step in the DNAJB12- and GABARAP-dependent autophagic disposal of dominantly toxic P23H-R.**

Monitoring Editor
Christian Ungermann
University of Osnabrück

Received: Oct 21, 2021
Revised: Jun 1, 2022
Accepted: Jun 8, 2022

This article was published online ahead of print in MBoC in Press (http://www.molbiolcell.org/cgi/doi/10.1091/mbc.E21-10-0505) on June 15, 2022.

*Address correspondence to: Douglas M. Cyr (DMCYR@med.unc.edu).

Abbreviations used: BafA1, bafilomycin A1; Bort, bortezomib; BSA, bovine serum albumin; CFTR, cystic fibrosis transmembrane conductance regulator; CMA, chaperone-mediated autophagy; 9CR, 9-cis-retinal; CRISPR, clustered regularly interspaced short palindromic repeats; DAPI, 4′,6-diamidino-2-phenylindole; DFCP1, Zinc finger FYVE domain-containing protein 1; DMEM, Dulbecco's Modified Eagle Medium; DTT, dithiothreitol; eGFP, enhanced green fluorescent protein; ER-phagy, ER-autophagy; ER, endoplasmic reticulum; ERAA, ER associated degradation; ERAD-RMP, ERAD-resistant membrane protein; ERAD, ER associated degradation; ERLAD, ER-to-lysosome-associated degradation; ERQC, ER quality control; GnRHR, Gonadotropin-releasing hormone receptor; GPCR, G-protein coupled receptor; IgG, immunoglobulin G; IPTG, isopropyl β-D-1-thiogalactopyranoside; JB12, DnaJ homolog subfamily B member 12; KO, knockout; LAMP, Lysosome-associated membrane glycoprotein 1 and/or 2; LIR, LC3 interacting region; P23H-R, P23H-rhodopsin; PB, sodium phosphate buffer; PBS, phosphate buffered saline; PBST, PBS with Triton X-100; PM, plasma membrane; PMSF, phenylmethylsulfonyl fluoride; PtdIns3P, phosphatidylinositol 3-phosphate; qPCR, quantitative polymerase chain reaction; QPD, Q to H mutant in HPD motif; SDS–PAGE, sodium dodecyl sulfate–polyacrylamide gel electrophoresis; siRNA, small interfering RNA; TEM, transmission electron microscopy; UPR, unfolded protein response; WIPI, WD repeat domain phosphoinositide-interacting protein; WT-R, wild type rhodopsin; WT, wild type.

INTRODUCTION

The endoplasmic reticulum (ER) is the site where biogenesis of membrane proteins initiates in a process that requires the coordinated folding and assembly of subdomains that are located in the cytosol, lumen, and ER membrane (Phillips and Miller, 2021). This process can be inefficient for both wild-type (WT) and disease proteins, which challenge ER protein quality control (ERQC) systems with the accumulation of potentially toxic misfolded intermediates (Hipp *et al.*, 2019). For example, retinitis pigmentosa arises from missense mutations in the light sensor rhodopsin that lead to its misfolding and retention in the ER. Rhodopsin is a G protein–coupled receptor (GPCR) that contains a conserved disulfide whose formation is required for binding of the light-sensing cofactor 9-cis-retinal (9CR) (Athanasiou *et al.*, 2018). Folding of rhodopsin, therefore, involves the initial collapse of its glycosylated nascent chains, disulfide bond formation, and cofactor binding. This stepwise process is facilitated by the glycan binding and ER transmembrane molecular chaperone calnexin, as well as cytosolic Hsp40 and Hsp70 chaperone pairs that function on the cytoplasmic face of the ER (Saliba *et al.*, 2002; Chapple and Cheetham, 2003).

The majority of nascent misfolded membrane proteins are cleared via ER-associated degradation (ERAD) involving their ER retention, ubiquitination, retrograde translocation to the cytosol, and

proteasomal degradation (Ferro-Novick *et al.*, 2021). Misfolded rhodopsin is a client of the ERAD pathway, but some rhodopsin mutants that cause retinitis pigmentosa, such as P23H-rhodopsin (P23H-R), are inefficiently degraded by ERAD (Jastrzebska *et al.*, 2006; Chiang *et al.*, 2012; Meng *et al.*, 2020). The resultant accumulation of dominantly toxic conformers of P23H-R causes retinal degeneration and blindness (Athanasiou *et al.*, 2018). How to therapeutically suppress mutant rhodopsin proteotoxicity remains to be discovered, and no drugs are available to treat the underlying cause of retinitis pigmentosa (Meng *et al.*, 2020).

To develop approaches that alleviate protein misfolding diseases such a retinitis pigmentosa, the identification of cellular mechanisms that buffer the accumulation of toxic protein species in the ER membrane system and secretory pathway is essential. Recent studies have identified selective autophagy mechanisms that operate in unstarved cells and clear misfolded and ERAD-resistant protein intermediates from the ER lumen, ER exit sites, and ER membrane (Wilkinson, 2019, 2020; Ferro-Novick *et al.*, 2021). ERAD-resistant forms of misfolded α-1-antitrypsin mutants are cleared from the ER lumen by complexes containing calnexin and the ER-autophagy (ER-phagy) receptor FAM134B (Fregno and Molinari, 2019) in a process termed ER-to-lysosome-associated degradation (ERLAD). Misfolded proteins that enter ER exit sites but cannot be secreted are degraded by microER-phagy in a FAM134B-dependent process. This process is thought to involve vesicle-mediated movement of misfolded and ERAD-resistant proteins that are stuck in ER exits to lysosomes (Loi and Molinari, 2020). ERAD-resistant misfolded membrane proteins accumulating in ER membranes are degraded via a pathway that is independent of FAM134B but requires the transmembrane Hsp40 DNAJB12 (JB12) and cytosolic Hsp70 that is referred to as ER-associated autophagy (ERAA) (Houck *et al.*, 2014; He, Houck, Kennedy, *et al.*, 2021).

Studies on the gonadotropin hormone releasing hormone receptor (GnRHR), a GPCR, demonstrated that the mutation E90K causes folding defects that occur downstream of the formation of the conserved disulfide that mediates formation of its ligand binding site (Houck *et al.*, 2014). This causes ERAD-resistant pools of E90K-GnRHR to accumulate in the ER and activates JB12/Hsp70-dependent ERAA (Houck *et al.*, 2014). Kinetically-trapped and ERAD-resistant intermediates of misfolded CFTR (cystic fibrosis transmembrane conductance regulator) have also been shown to be cleared from the ER via ERAA (He, Houck, Kennedy, *et al.*, 2021). Kinetically-trapped intermediates of membrane proteins that are resistant to ERAD (ERAD-RMPs) accumulate in ER membranes because they cannot be unfolded and retrotranslocated to the cytosol (Fujita *et al.*, 2007; Chiang *et al.*, 2012; Houck *et al.*, 2014; He, Houck, Kennedy, *et al.*, 2021). This invites them to remain associated with JB12 and Hsp70 for extended times, leading to downstream association of JB12 and Hsp70 with autophagy initiation machinery (Houck *et al.*, 2014; He, Houck, Kennedy, *et al.*, 2021). These events are proposed to drive the metamorphosis of ER tubules containing ERAD-RMPs into phagophores (autophagosome precursors) within omegasomes (autophagy initiation sites) that are decorated with the phosphatidylinositol 3-phosphate (PtdIns3*P*) binding protein WIPI1 (WD-repeat protein interacting with phosphoinositides) (Proikas-Cezanne *et al.*, 2004, 2007; Proikas-Cezanne and Pfisterer, 2009; He, Houck, Kennedy, *et al.*, 2021). Yet it is currently not clear how ERAD-RMPs are packaged into autophagosomes and transferred from the ER to lysosomes (Ferro-Novick *et al.*, 2021).

Herein, we report on the study of the mechanisms for the triage by the JB12/Hsp70 chaperone complex of WT rhodopsin (WT-R) and P23H-R for degradation via ERAD or ERAA within the ER membrane system. This process does not require known ER-phagy receptors (He, Houck, Kennedy, *et al.*, 2021) and is an alternative to the ERAD pathway, so it is referred to as ER-associated autophagy (ERAA). Both WT-R and P23H-R were detected in complexes with JB12 and Hsp70, with levels of P23H-R:JB12 complexes being dramatically higher than those with WT-R. P23H-R accumulates in ER tubules with JB12 that interact with components of omegasome rings DFCP1 (double FYVE domain–containing protein) and WIPI1 that bind PtdIns3*P* produced by the Beclin-1:VPS34 autophagy initiation kinase (Ferro-Novick *et al.*, 2021). P23H-R, but not WT-R, also accumulated in lysosomes with ATG8 family members and the lysosome marker LAMP. Interference with the folding of P23H-R via mutation of the highly conserved cysteines that form rhodopsin's disulfide bridge prevented P23H-R entry into omegasomes, so the conformation of misfolded rhodopsin is fate determining. ER tubules enriched in P23H-R and containing GABARAP extend into the cytosol from WIPI1-decorated rings of ER membrane. Lysosomes transiently dock with WIPI1 rings and then become enveloped by phagophores containing P23H-R. Lysosomes are detected in association with 10% of all cellular WIPI1 foci. P23H-R expression stimulates the association of lysosomes with WIPI1 foci 2.5-fold. Lysosome docking to WIPI1 occurs for 10–70 s. After lysosome departure from WIPI, patches of P23H-R are detected in the membranes of lysosomes. The depletion of GABARAP prevents transfer of P23H-R from the ER to lysosomes but does not hinder the sequestration of P23H-R into phagophores, nor lysosome docking to WIPI1 rings. Models for the sequential roles of JB12 and Hsp70, GABARAP, and lysosome docking to WIPI1 rings in the clearance of ERAD-resistant and dominantly toxic pools of P23H-R from the ER tubular network by ERAA will be discussed.

RESULTS

Triage of P23H-rhodopsin between proteasomal and lysosomal degradation is conformation dependent

To explore the mechanism for triage in the ER of misfolded rhodopsin intermediates, we evaluated the fate of WT-R and P23H-R through microscopy and biochemical methods (Figure 1). WT-R and P23H-R behave similarly to WT-R-eGFP and P23H-R-eGFP in biochemical and cell biological assays that monitor their biogenesis (Saliba *et al.*, 2002; Chapple and Cheetham, 2003). We therefore employed eGFP-tagged forms of WT-R and P23H-R in our studies and from here on we refer to the eGFP-tagged proteins as WT-R and P23H-R.

To investigate mechanisms for triage of rhodopsin intermediates, we used experimental conditions where WT-R and P23H-R were expressed from 50–100 ng of the same expression plasmid as that used in previous studies which suggested that P23H-R is aggregation prone and becomes sequestered within aggresomes (Saliba *et al.*, 2002; Park, 2019). Under these conditions, P23H-R is biosynthesized at low levels that do not strongly induce the unfolded protein response (UPR) (Supplemental Figure S1B). It is also within the cellular capacity for WT-R to accumulate at the plasma membrane (PM), with low levels detected in the ER membrane with calnexin (Figure 1A). In contrast, P23H-R colocalizes primarily with calnexin and the lysosome-associated membrane protein 2 (LAMP2) (Figure 1A). (LAMP1 and LAMP2 are both lysosome makers and recognized by different mouse monoclonal antibodies, so they are used interchangeably and are denoted as LAMP.) Because WT-R is endocytosed from the PM, a pool of it is detected in lysosomes, but colocalization of P23H-R with LAMP occurs at a higher degree than for WT-R (Figure 1A). Because P23H-R is retained in the ER, its route for traffic to the lysosome is different from the route for WT-R.

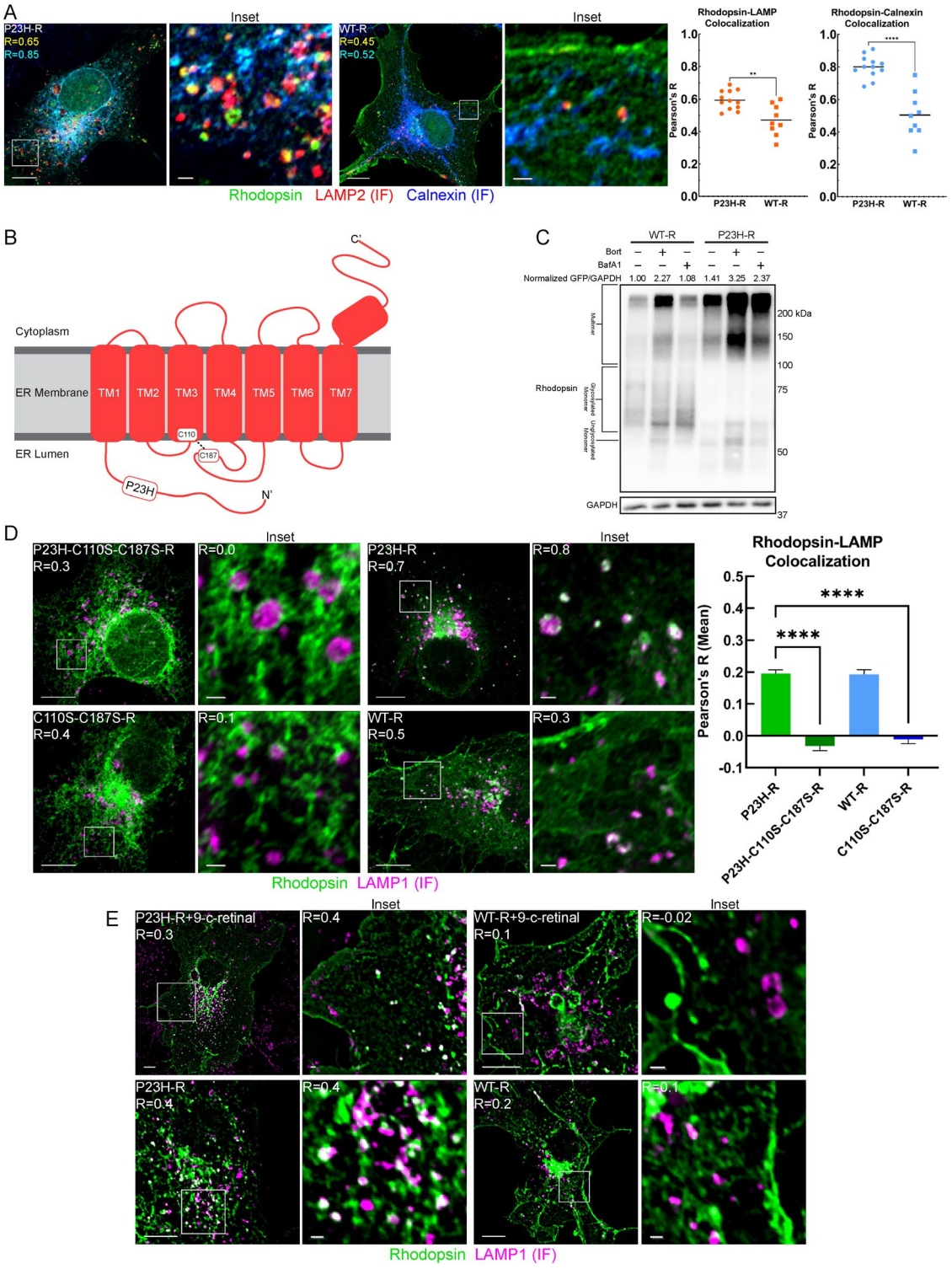

FIGURE 1: P23H-rhodopsin triage between the proteasome and lysosome. COS-7 cells transiently transfected with eGFP-rhodopsin WT or the indicated mutations. All microscopy conducted in fixed cells with immunofluorescence staining for the indicated marker. (A) Left: Fixed-cell confocal microscopy with Airyscan: LAMP2a (red), rhodopsin (green), and calnexin (blue). Pearson's *R* values indicated in whole-cell panels by color: top number (yellow) LAMP-Rho; bottom number (cyan) calnexin-Rho. Right: Dot plots of Pearson's *R* with unpaired *t* test: line indicates mean. (B) Illustration of rhodopsin secondary structure. (C) Western blot of COS-7 cells expressing either WT-R or P23H-R and treated with either 10 μM Bort or 100 nM BafA1 for 6 h. (D) Left: Fixed-cell confocal microscopy with Airyscan of the indicated rhodopsin mutant: rhodopsin (green), LAMP1 (magenta). *R* indicates Pearson's *R* for rhodopsin-LAMP1 colocalization. Right: Bar graph of mean Pearson's *R* values between rhodopsin and LAMP1 calculated within identified LAMP1 objects. Kruskal–Wallis and Dunn's multiple comparisons tests ($n = 1240$). Error bars for SEM. (E) Fixed-cell epifluorescence microscopy of WT-R or P23H-R ± 10 μM 9CR for 6 h: rhodopsin (green), LAMP1 (magenta). *R* indicates Pearson's *R* for rhodopsin-LAMP1 colocalization. $^{**}P < 0.01$, $^{****}P < 0.0001$. Scale bars: whole-cell views = 10 μm; insets = 1 μm.

Through measurement of P23H-R expression by microscopy, accumulation in lysosomes was concentration independent (Supplemental Figure S1A). Rhodopsin is expressed at high levels within the inner segment of rod cells and represents up to 90% of total protein within photoreceptor discs of the outer segment (Meng *et al.*, 2020). Thus, under the experimental conditions utilized, the overexpression of WT-R and P23H-R permits study of basic mechanisms for triage of nascent and misfolded rhodopsin between folding or degradation.

To biochemically evaluate the route for degradation of WT-R and P23H-R, we tested the sensitivity of their steady-state accumulation to the proteasome inhibitor bortezomib (Bort) and the lysosomal proton pump inhibitor bafilomycin A1 (BafA1). BafA1 increases the pH of the lysosome lumen and thereby renders lysosomal endoproteases inactive. WT-R and P23H-R ran on SDS–PAGE gels with different mobilities that correspond to a faster glycosylated ER pool, a slower heavily glycosylated form trafficked to the PM, or multimers that form after cell lysis. Because WT-R and P23H-R self-associate and migrate as higher molecular weight oligomers during SDS–PAGE, we quantitated the signals for the entire lane on western blots of cell lysates. Folding of WT-R is inefficient, with misfolded intermediates being degraded by ERAD (Saliba *et al.*, 2002; Chapple and Cheetham, 2003). Incubation of cells with Bort for 6 h before harvest caused a greater than twofold increase in WT-R accumulation, but BafA1 did not increase WT-R accumulation. Bort acted to increase P23H-R accumulation around twofold as did BafA1 (Figure 1C). These data are consistent with imaging data showing P23H-R accumulation in both the ER with calnexin and in lysosomes with LAMP. These results are also consistent with previous studies on the triage of misfolded membrane proteins showing that the conformation of membrane protein intermediates is scanned on an individual basis for triage to pathways for proteasomal or lysosomal degradation (Fujita *et al.*, 2007; Chiang *et al.*, 2012; Buchberger, 2014; Houck *et al.*, 2014; He, Houck, Kennedy, *et al.*, 2021).

Models for membrane protein triage suggest that pools of ER-arrested intermediates contain globally misfolded conformers that are retrotranslocated for ERAD. There is also a population of kinetically-trapped intermediates containing stable tertiary structure causing resistance to retrotranslocation and triage for lysosomal degradation (Houck *et al.*, 2014; He, Houck, Kennedy, *et al.*, 2021). The cysteine residues C110 and C187 in rhodopsin form a highly conserved and stabilizing disulfide in GPCR biogenic intermediates (Conn *et al.*, 2007). We therefore asked whether destabilization via mutating C110 and C187 to serine would impact the degradation fate of P23H-R. C110S-C187S-R did not traffic to the cell surface, indicative of it having a nonnative conformation. P23H-C110S-C187S-R showed a reduced propensity to accumulate in lysosomes with LAMP when compared with P23H-R (Figure 1D). To verify this observation, we employed object-based identification of LAMP vesicles (n = 1240) with subsequent correlation coefficient calculations (Pearson's R) between LAMP and the indicated rhodopsin mutant. Mean Pearson's R values were significantly different when comparing P23H-C110S-C187S-R (mean R = –0.004) and P23H-R (mean R = 0.36), confirming a dramatic reduction in traffic to lysosomes.

To evaluate how the stabilization of P23H-R impacts triage decisions, 9CR, the chromophore of rhodopsin known to act as a pharmacologic chaperone (Chen *et al.*, 2014; Meng *et al.*, 2020), was included for 6 h in cell culture media before fixation. Imaging revealed that 9CR promotes cell-surface localization of a fraction of P23H-R, indicating suppression of misfolding. P23H-R and LAMP colocalization was still detected in 9CR-treated cells (Figure 1E). 9CR binding appears to stabilize ER pools of P23H-R but cannot prevent formation of ERAA-targeted conformers. These collective data suggest that kinetically-trapped intermediates of P23H-R, which have stable but nonnative structure, are triaged for lysosomal degradation.

Lysosomal degradation of P23H-rhodopsin is facilitated by the ER-associated chaperones JB12 and Hsp70

JB12 and cytosolic Hsp70 dynamically interact with different ERQC machineries during the conformation-dependent triage of membrane proteins between assembly into active conformers, or degradation via the proteasome or lysosome (Grove *et al.*, 2011; Houck *et al.*, 2014; Walczak *et al.*, 2014; Li *et al.*, 2017; He, Houck, Kennedy, *et al.*, 2021). To determine the requirements for JB12 in the conformation-dependent triage of rhodopsin intermediates, the localization of endogenous JB12 with P23H-R or P23H-C110S-C187S-R was imaged. Both P23H-R and the destabilized P23H-C110S-C187S-R colocalized with JB12 in the ER (Figure 2A). Notably, the P23H-R signal that colocalized with JB12 was also seen in connected ER-membranes containing P23H-R but devoid of JB12. This arrangement was not observed with P23H-C110S-C187S-R. These data suggest that P23H-R is segregated within the ER into JB12-free and JB12-bound pools, and below we define the importance of this segregation event in triage of P23H-R.

To determine whether the ER transmembrane chaperone JB12 is an integral participant in the P23H-R triage mechanism, a knockout cell line (JB12-KO) was generated using the CRISPR/Cas9 system in HeLa cells. Depletion of JB12 was confirmed by western blot (Supplemental Figure S2A) and immunostaining in fixed-cell microscopy (Figure 2B). CRISPR-Control and JB12-KO knockdown cells were transiently transfected with P23H-R and imaged. JB12 knockout impaired accumulation of P23H-R in lysosomes (Figure 2B). Object-based image analysis of LAMP vesicles in CRISPR-Control cells (n = 5796) and JB12-KO cells (n = 3789) reveals that the loss of JB12 reduced P23H-R presence in lysosomes (Figure 2B). Importantly, endogenous LC3b retained its localization to the lysosome, indicating that basal autophagy still occurs in the absence of JB12 (Figure 2B).

It remained unclear whether JB12 influenced P23H-R triage directly or indirectly, so their presence in complexes with each other was evaluated. FLAG-JB12 was introduced into cells that were challenged with P23H-R or P23H-C110S-C187S-R. Both P23H-R and P23H-C110S-C187S-R were present in FLAG-JB12 immunoprecipitates with Hsp70, but the ER transmembrane chaperone calnexin was absent (Figure 2C).

To test the functional importance of JB12's interaction with Hsp70 in triage events, P23H-R was coexpressed with either WT JB12 or QPD-JB12. QPD-JB12 is a dominant-negative mutant that binds nonnative clients and interacts with protein homeostatic machinery, but its Hsp70 binding domain is defective due to a Q to H mutation in its HPD motif. QPD-JB12 is incapable of functional interactions with Hsp70, so it binds nonnative clients and blocks their downstream binding to Hsp70 (Grove *et al.*, 2011; He, Houck, Kennedy, *et al.*, 2021). Western blot analysis revealed a greater than fourfold increase in P23H-R steady-state levels in the presence of QPD-JB12, whereas elevation of WT-JB12 reduced steady-state levels (Figure 2D). Notably, QPD-JB12 associates with P23H-R at higher levels than WT-JB12 (Figure 2E) and does not cause P23H-R to enter detergent-insoluble aggregates (Supplemental Figure S2B). Imaging of cells coexpressing P23H-R and QPD-JB12 showed reduced colocalization of P23H-R with lysosomes and retention in the ER (Supplemental Figure S2D).

In cells that express dominant-negative mutant forms of the core autophagy initiation kinase ULK1 (Unc-51–like autophagy-activating kinase) or Beclin-1, the scaffold for the class III PtdIns3*P* kinase

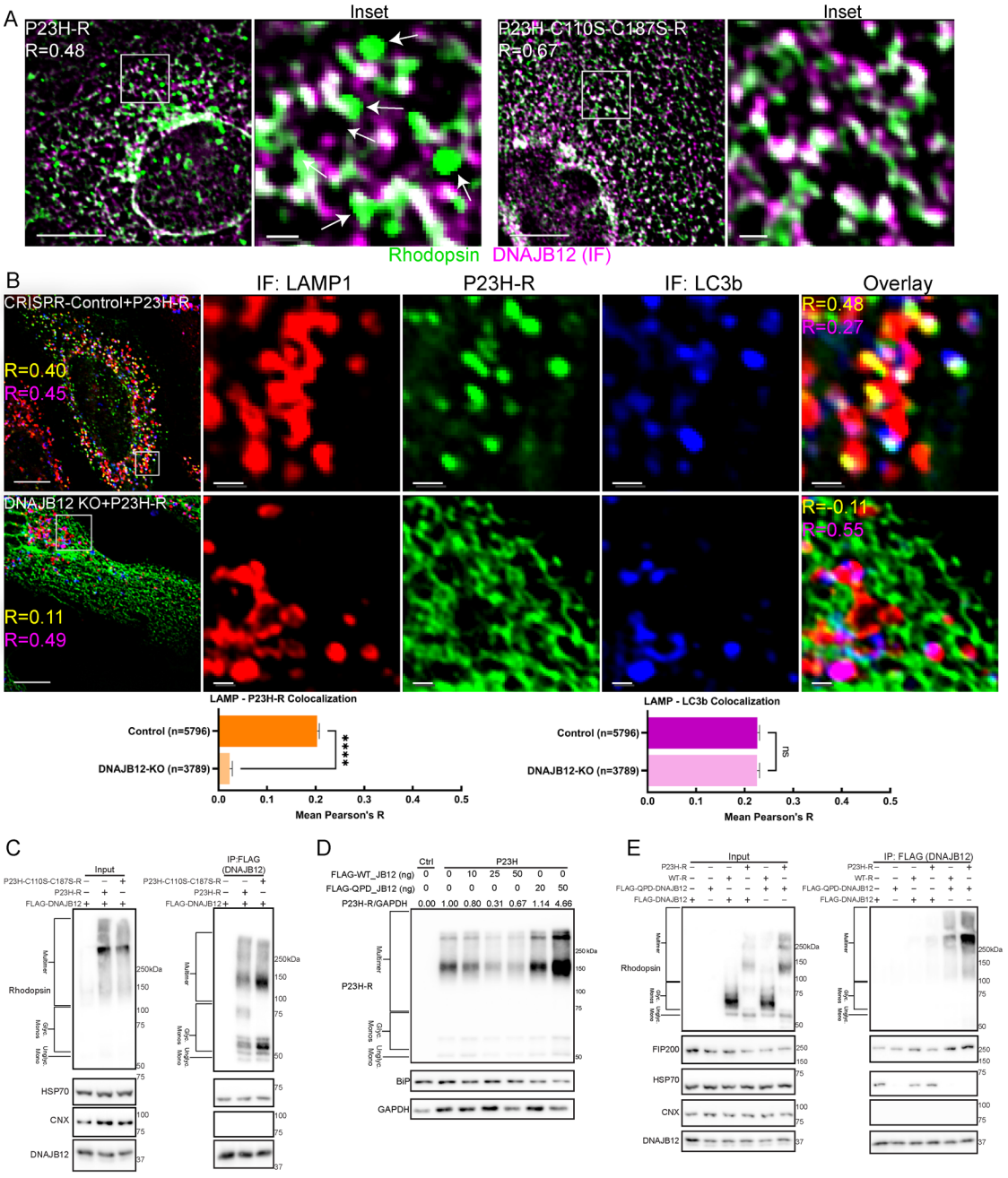

FIGURE 2: DNAJB12 and HSP70 participate in the triage of misfolded P23H-rhodopsin toward lysosomal degradation. (A) Fixed-cell epifluorescence microscopy of COS-7 cells transiently transfected with P23H-R or P23H-C110S-C187S-R and immunostained for DNAJB12. Green: rhodopsin; magenta: DNAJB12; white arrows: P23H-R foci extending from the ER tubules containing DNAJB12. *R* indicates Pearson's *R* for rhodopsin-DNAJB12 colocalization. (B) Fixed-cell epifluorescence microscopy of HeLa cell lines transduced with either a control (CRISPR-Control) or DNAJB12 knockout (CRISPR DNAJB12 KO) and then transiently transfected with P23H-R. Top: Immunofluorescence conducted for LAMP1 (red) or LC3b (blue). *R* values: top (yellow) P23H-R-LAMP1; bottom (magenta) LAMP1-LC3b. Bottom: Bar graphs of mean Pearson's *R* values between rhodopsin and LAMP1 (left) or LAMP1 and LC3b (right) calculated within the identified LAMP1 objects. Mann–Whitney test; error bars for SEM. (C) Western blot of FLAG pull down in COS-7 cells transiently transfected with FLAG-DNAJB12 and either P23H-R or P23H-C110S-C187S-R. (D) Western blot of COS-7 cells transiently transfected with P23H-R and increasing concentrations of either FLAG-DNAJB12 (WT) or FLAG-QPD-DNAJB12 (DNAJB12 mutant with dominant-negative HSP70 interaction domain). (E) Western blot of FLAG pull down in HeLa cells transiently transfected with P23H-R or WT-R and either FLAG-DNAJB12 or FLAG-QPD-DNAJB12. ****$P <$ 0.0001. Scale bars: whole-cell views = 10 µm; insets = 1 µm.

VPS34, entry of P23H-R into lysosomes with LAMP is impaired (Supplemental Figure S2E). Likewise, treating cells with the ULK1 inhibitor MRT-68921 (Supplemental Figure S2, F and G) (Petherick *et al.*, 2015) or the VPS34 inhibitor PIK-III (Supplemental Figure S2C) (Dowdle *et al.*, 2014) caused a significant decrease in P23H-R colocalization with LAMP (Supplemental Figure S2). JB12 and Hsp70 are

present in complexes with P23H-R and function in a pathway requiring the canonical autophagy initiation factors ULK1 and Beclin-1 to triage P23H-R intermediates for degradation via ERAA.

FIP200 (focal adhesion kinase family interacting protein of 200 kDa) localizes on intracellular membranes to target its partner, ULK1, to focally initiate selective autophagy (Ravenhill *et al.*, 2019; Vargas *et al.*, 2019). Hsp70 and Hsp40s cooperate with Hsp90 to regulate the activity of kinases that include ULK1 (Joo *et al.*, 2011). It is possible that interaction of JB12 with FIP200 could target sites in the ER where ERAA initiates. To address this possibility, we conducted FLAG-JB12 immunoprecipitations from extracts of cells expressing P23H-R. FIP200 and Hsp70 were present in the products of FLAG-JB12 pull downs. Levels of FIP200 and P23H-R were elevated in immunoprecipitates with FLAG-QPD-JB12, but Hsp70 was absent (Figure 2E). Thus, JB12 is detected in association with FIP200, Hsp70, and P23H-R. QPD-JB12 might inhibit ERAA because it sequesters FIP200 in complexes that cannot be activated due to the absence of Hsp70. The association of FIP200 in complexes with JB12 and P23H-R suggests a potential role for JB12 in local regulation of FIP200/ULK1 function in ER microdomains where ERAD-RMPs accumulate. These data support the concept that JB12 participates in the focal regulation of ERAD-RMP traffic via ERAA to lysosomes (Houck *et al.*, 2014; He, Houck, Kennedy, *et al.*, 2021).

P23H-rhodopsin intermediates accumulate in both the lysosome membrane and lumen

Challenge to the ER during starvation, oxidative stress, and proteotoxicity is managed by a collection of ER-phagy receptors that have unique domain structures and localization within the ER tubular network (Wilkinson, 2019; Chino and Mizushima, 2020; Loi and Molinari, 2020; Ferro-Novick *et al.*, 2021). ER-phagy receptors contain an LC3 interacting region (LIR) that is recognized by the autophagy gene 8 (ATG8) subfamilies LC3 and GABARAP. ATG8s are conjugated to head groups of lipids on the surface of phagophore membranes (autophagosome precursors). ER-phagy receptor binding to lipidated ATG8s serves to target damaged ER fragments to phagophore membranes and entrap damaged ER fragments within the lumen of autophagosomes (Wilkinson, 2019; Chino and Mizushima, 2020; Loi and Molinari, 2020; Ferro-Novick *et al.*, 2021). Interestingly ERAD-RMPs are detected in both the lumen and membranes of lysosomes, suggesting that their route to lysosomes is different from the paths taken by cargo of known ER-phagy receptors (Houck *et al.*, 2014; Loi and Molinari, 2020; Ferro-Novick *et al.*, 2021; He, Houck, Kennedy, *et al.*, 2021).

This supposition was evaluated through study of P23H-Rs' route of passage from the ER to lysosomes. We started at the endpoint and examined the localization of P23H-R within lysosomes of fixed and live cells. Based on models for ER-phagy, it was anticipated that dominantly toxic P23H-R would localize with calnexin in damaged ER fragments found in the lysosome lumen. Instead, in both live and fixed cells, P23H-R accumulates with LAMP in membranes of lysosomes and also the lumen, but calnexin does not colocalize in the lumen with P23H-R (Figures 1A, 2A, 3, A–C, Supplemental Figure S3B, and below). The addition of BafA1 to cells for 6 h before fixation caused lysosomes to expand, making it easier to visualize the accumulation of P23H-R signals with LAMP (Supplemental Figure S3B). P23H-R localization in lysosomes was also readily detected by immunofluorescence staining for GFP (Figure 3A). Data from transmission electron microscopy (TEM) on eGFP-P23H with immunogold staining for eGFP also reveal signals in both the lysosome membrane and lumen (Supplemental Figure S3A). Notably, P23H-R signals are absent from ER whorls, a marker for ER fragments in TEM (Supplemental Figure S3A). Under growth conditions utilized, P23H-R expression does not induce the unfolded protein response, and lysosomal ER fragments detected by TEM did not contain P23H-R (Figure 3B and Supplemental Figures S1B and S3A).

Next, it was asked whether the induction of a known ER-phagy route would affect the localization of P23H-R within lysosomes (Figure 3C). To induce ER-phagy, we overexpressed the abundant autophagy receptor TEX264, which contains a cytosolic intrinsically disordered domain that could facilitate interactions with misfolded membrane proteins (An *et al.*, 2019; Chino *et al.*, 2019; Delorme-Axford *et al.*, 2019). P23H-R was imaged with LAMP, endogenous calnexin, and TEX264. In control cells, P23H-R signals were detected in the lysosome membrane and lysosome lumen. In the control, signals for calnexin were absent from the lysosome (Figure 3, C–E). Expressing exogenous TEX264-HaloTag induced ER-phagy, causing calnexin to accumulate in lysosomes. TEX264 expression also caused an increase in the signal for lumenal P23H-R localization, which was now observed to colocalize in the lumen with calnexin and TEX264 (Figure 3, C and D).

In the lysosomes of biosynthetically active cells, signals for P23H-R accumulate in the lysosome membrane and lumen, with signals being absent for the ER transmembrane chaperone calnexin, a result suggesting that P23H-R is segregated away from calnexin within the ER before it is transferred to lysosomes. Induction of ER-phagy by elevation of TEX264 appears to alter the route taken by P23H-R to lysosomes because it reduces P23H-R colocalization with LAMP and causes a corresponding colocalization of P23H-R with calnexin in the ER lumen (Figure 3C). These data are consistent with there being more than one route for traffic of damaged proteins and ER membranes from the ER membrane system to LAMP-positive lysosomes (Houck *et al.*, 2014; Bhaskara *et al.*, 2019; Chen *et al.*, 2019; Chino *et al.*, 2019; Ferro-Novick *et al.*, 2021). The sorting of P23H-R from the ER to lysosomes is conformation dependent, involves JB12 and Hsp70 segregation of endogenous calnexin away from P23H-R, and results in the accumulation of P23H-R in the lysosome membrane and lumen.

To evaluate the potential role of selective ER-phagy receptors in P23H-R triage, we used CRISPR/Cas9 and small interfering RNA (siRNA) to deplete six of the known ER-phagy receptors alone and all together (Wilkinson, 2019; Chino and Mizushima, 2020; Loi and Molinari, 2020; Ferro-Novick *et al.*, 2021) (Figure 3, E and F, and Supplemental Figure S3, D–I). The impact that loss of each respective ER-phagy receptor had on the colocalization between P23H-R and LAMP was evaluated by Pearson's correlation across 441 cells. Each respective knockdown cell line failed to exhibit a statistically significant difference, showing that the individual depletion of the ER-phagy receptors under study did not affect P23H-R accumulation in lysosomes (Figure 3, E and F, and Supplemental Figure S3, D–I). In addition, simultaneous knockdown of all six ER-phagy receptors still supported the accumulation of P23H-R within lysosomes (Figure 3F). These collective data suggest an ER exit mechanism for selective autophagy of P23H-R that is distinct from events that involve the engulfment by phagophores of ER membranes containing P23H-R and a particular ER-phagy receptor. Yet it remains possible that this process does require action of an autophagy receptor that is yet to be uncovered.

P23H-R intermediates localize within omegasomes during passage from the ER to lysosomes

The presence of P23H-R in both the membrane and lumen of lysosomes suggests a model in which ER tubules that contain P23H-R are the source of the phagophore and autophagosome membranes that deliver P23H-R to lysosomes. In this scenario, ERAD-RMPs

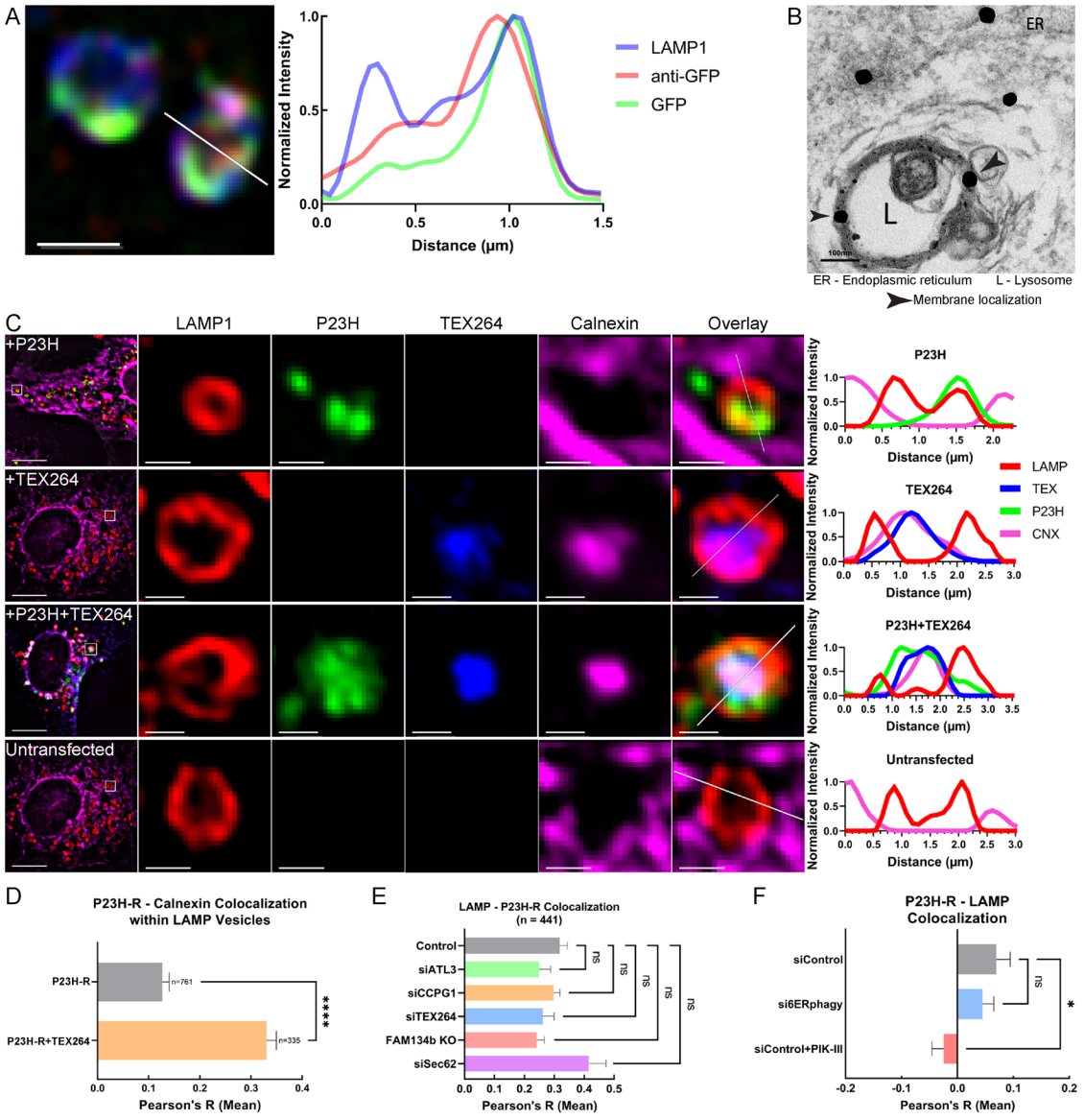

FIGURE 3: P23H-rhodopsin is trafficked independent of ER-phagy indicators. (A) Fixed-cell confocal microscopy with Airyscan of COS-7 cells transiently transfected with P23H-R (green), treated with BafA1, and immunostained for GFP (red) or LAMP1 (blue). (B) TEM image of anti-GFP immunogold staining in COS-7 cells transiently transfected with P23H-R (P23H-Rhodopsin-eGFP) with no pharmacological treatments. Scale bar = 100 nm. (C) Left: Fixed-cell epifluorescence microscopy: COS-7 cells were transiently transfected with either P23H-R (green), TEX-164-HaloTag (blue), or both and then incubated with 50 nM Janelia Fluor 646 HaloTag Ligand (blue) and 100 nM BafA1, followed by fixation and immunofluorescence staining for LAMP1 (red) or calnexin (magenta). Right: Plot profiles for line drawn in inset overlay. (D) Bar graph of mean Pearson's *R* values between rhodopsin and calnexin calculated within the identified LAMP1 objects from C. Mann–Whitney test ($n = 1096$; error bars for SEM). (E, F) Mean of Pearson's *R* for each indicated condition (error bars for SEM). (E) All ER-phagy receptors were knocked down by siRNA except for FAM134B which used a CRISPR knockout cell line generated via lentiviral transduction. Kruskal–Wallis and Dunn's multiple comparisons tests. (F) Simultaneous siRNA (si6ERphagy) for *CCPG1, SEC62, RETREG1, TEX264, RTN3, ATL3*; $n = 135$ cells. One-way analysis of variance with multiple comparisons. $^*P < 0.05$, $^{****}P < 0.0001$. Scale bars (unless indicated): whole-cell views = 10 μm; insets = 1 μm.

would be present in both autophagosome membranes, with the outer membrane containing P23H-R being fused with the lysosome membrane and P23H-R in the inner membrane being delivered to the lysosome lumen. If this model is accurate, then ER tubules containing P23H-R should associate with omegasomes and be converted into phagophores.

Consistent with the concept that JB12 facilitates the conversion of ER tubules containing ERAD-RMPs into phagophores, we detect the colocalization of endogenous JB12 in discrete foci with endogenous pools of the ULK1 kinase targeting subunit, FIP200, that form at the edge of a larger membrane surface enriched in P23H-R (Figure 4A). P23H-R foci of different sizes that are enriched in endogenous JB12 colocalize on the edge and in the center of omegasomes containing a discrete set of endogenous WIPI1-decorated ER tubules (Supplemental Figure S4C). WIPI proteins bind PtdIns3*P* head groups on lipids produced by VPS34 autophagy initiation kinase

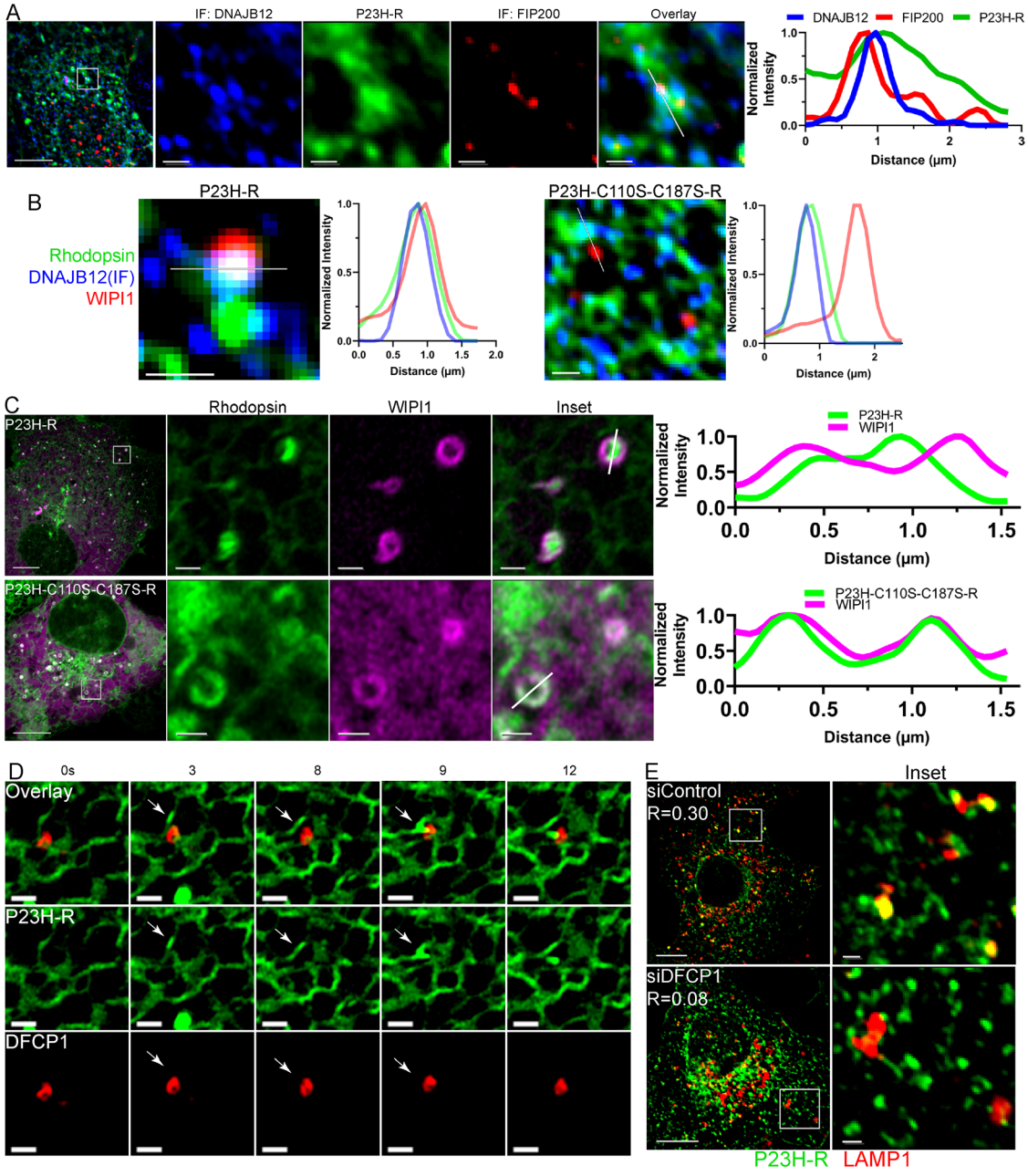

FIGURE 4: P23H-rhodopsin localizes to omegasome markers. (A, B) Fixed-cell epifluorescence microscopy of COS-7 cells transiently transfected with P23H-R and immunostained for the indicated marker. Right: Plot profile for line drawn in inset overlays. (B) The indicated rhodopsin mutant coexpressed with WIPI1-mCherry. Scale bar = 1 μm. (C) Left: Live-cell confocal microscopy of COS-7 cells expressing WIPI1-mCherry and either P23H-R or P23H-C110S-C187S-R. Right: Plot profile of line drawn in inset overlay. (D) Time lapse of live-cell confocal microscopy of COS-7 cells expressing DFCP1-mCherry and P23H-R. Scale bar = 1 μm. (E) Fixed-cell epifluorescence microscopy of COS-7 cells expressing P23H-R after siControl or siDFCP1 knockdown. Scale bars (unless indicated): whole cell views = 10 μm; insets = 1 μm.

complexes that are activated by ULK1/FIP200 complexes (Proikas-Cezanne *et al.*, 2004, 2007; Proikas-Cezanne and Pfisterer, 2009). When observing nascent WIPI foci that have not matured into characteristic omagasomal rings, P23H-R is seen to colocalize with WIPI1 and JB12. In contrast, P23H-C110S-C187S-R colocalizes with JB12 but does not associate with membranes decorated with endogenous WIPI1 (Figure 4B). In live cells that express WIPI1-mCherry and P23H-R, a signal for P23H-R localizes in the center of WIPI rings (Figure 4C). In contrast, P23H-C110S-C187S-R did not localize inside WIPI1 rings but did colocalize with WIPI1 (Figure 4C). This colocalization is expected because P23H-C110S-C187S-R is present in ER membranes and some of these are painted with WIPI1, but globally misfolded P23H-C110S-C187S-R does not accumulate within omegasomes decorated by WIPI1 (Figure 4C). WIPI1 is demonstrated to decorate ER tubules that associate with independent P23H-R–containing ER tubules, suggesting that P23H-R degradation intermediates pass through omegasomes en route to the lysosome.

Double FYVE-containing protein 1 (DFCP1) also binds PtdIns3*P* lipid head groups and acts alongside WIPI proteins during omegasome biogenesis and initiation of autophagy (Derubeis *et al.*, 2000;

Tooze and Yoshimori, 2010). In live cells, DFCP1 rings were of sizes similar to those of WIPI1 rings and contained P23H-R–enriched ER membranes (Supplemental Figure S4B). In time-course imaging studies, at $t = 3$ and 8 s an ER tubule containing P23H-R is seen adjacent to a DFCP1 ring. At $t = 9$ s a portion of the tubule contacts the DFCP1 ring. Thus, ER tubules containing P23H-R dynamically interact with omegasomes. Because there are four WIPI family members in primate cells (Proikas-Cezanne *et al.*, 2004; Thurston *et al.*, 2016; De Leo *et al.*, 2021), we were not able to deplete all members of the WIPI family to levels that block basal autophagy or ERAA (unpublished data). Only two DFCP homologues are expressed in mammals (Derubeis *et al.*, 2000), and siRNA depletion of DFCP1 was sufficient to impair the accumulation of P23H-R in lysosomes (Figure 4E).

In biosynthetically active cells, ER tubules decorated with endogenous WIPI1 are routinely detected and this is consistent with the observed constitutive requirement for selective autophagy in cellular homeostasis (Ferro-Novick *et al.*, 2021). Independent ER tubules containing P23H-R, but not globally misfolded forms of P23H-R, associate with WIPI-decorated ER tubules. These data support a model in which ER tubules containing P23H-R interact with autophagy initiation machinery at omegasomes during autophagic transfer of P23H-R from the ER to lysosomes (Houck *et al.*, 2014; He, Houck, Kennedy, *et al.*, 2021).

Lysosomes dynamically dock with WIPI1 rings containing P23H-rhodopsin–enriched ER tubules

Next, we used fixed- and live-cell imaging to study the mechanisms for transfer of P23H-R from the ER to lysosomes (Figure 5). We stained fixed cells for endogenous WIPI1 and LAMP and probed the location of P23H-R. We anticipated that P23H-R–enriched autophagosomes would dock with lysosomes that are located in the vicinity of the centrosome (Pu *et al.*, 2016). Instead, we were surprised to observe the association of lysosomes with WIPI1 rings containing P23H-R (Figure 5A). These "docking events" were transient yet stable, with the longest association seen to last 70 s (Supplemental Figure S5A). Object-based detection of LAMP and WIPI1 foci showed 10% of the 9823 identified WIPI1 objects as overlapping with LAMP. In cells expressing P23H-R, 25% of the 743 WIPI1 objects overlapped with LAMP (Figure 5A). Thus, lysosomes dock to WIPI1 rings, and these interactions are stimulated up to 250% by the ERAA client P23H-R.

Images of live cells expressing WIPI1-mCherry, LAMP1-mTagBFP2, and P23H-R-eGFP permitted the capture of a three-dimensional view of the interface between WIPI1 rings, P23H-R phagophores, and lysosomes. Examination of a *z*-stack containing a WIPI1 ring and a docked lysosome suggests a potential mechanism by which P23H-R exits the ER during ERAA. Stepwise slices of the *z*-stack that are +0.9 to –0.9 µm above or below the center of the WIPI1 structure show that P23H-R is enriched in lysosomes that dock with one side of the WIPI1 ring at –0.3 to –0.9 µm (Figure 5B). Three-dimensional views of this processed *z*-stack are presented as superior, inferior, and lateral views (Figure 5C and Supplemental Figure S5B). The superior view displays a WIPI1 ring that is contacted along its exterior surface by P23H-R–enriched ER tubules. There is also a P23H-R–enriched ER membrane that coats the wall of the WIPI1 ring and then folds into its central cavity and then out the top. The inferior view displays a notch in the WIPI1 ring in which a lysosome has docked. The lateral view shows P23H-R that colocalizes with LAMP1 in lysosomes. We interpret these data to suggest that P23H-R–enriched ER tubules interact with omegasomal surfaces containing autophagy initiation machinery. These interactions then facilitate the metamorphosis of P23H-R tubules into phagophores that deliver their contents to lysosomes docked on the same WIPI1 ring.

To test this model, the dynamic association of lysosomes with WIPI1 rings containing P23H-R tubules was evaluated in a live *z*-stack acquisition over time (Figure 5D and Supplemental Figure S5C). Shown are images at $z = 0$, +0.3, and +0.6 µm between $t = 3$ and 20 s. A lysosome is seen separate, but nearby, an omegasome containing WIPI1 and P23H-R ($t = 3$ s), followed by its approach ($t = 4$ s) and then docking ($t = 8$–10 s) to the omegasome. The lysosome disengages ($t = 13$ s), moves away from the WIPI1 ring ($t = 15$ s), and now contains P23H-R in its membrane ($t = 20$ s). These collective data demonstrate the dynamic association of lysosomes with WIPI1 rings that contain an ERAA client. They support the interpretation that autophagic transfer of P23H-R out of the ER occurs during lysosome docking to WIPI1 rings.

GABARAP facilitates P23H-R exit from omegasomes and accumulation in lysosomes

The ER tubules containing P23H-R extend into the cytosol from omegasomes, and we surmise that these tubules are of ER-connected phagophores (Hayashi-Nishino *et al.*, 2009, 2010; Yla-Anttila *et al.*, 2009). We therefore evaluated the requirement of the ATG8 family members LC3a/b/c and GABARAP/L1/L2 in clearance of P23H-R from the ER. Unbiased object-based quantitation of more than 13,700 lysosomes showed that the simultaneous depletion of GABARAP, GABARAP-L1, and GABARAP-L2 by siRNA (siGABARAP/L1/L2) decreased the accumulation of P23H-R in lysosomes (Figure 6A and Supplemental Figure S6G). Importantly, siGABARAP/L1/L2 did not abolish LC3b accumulation in lysosomes (Supplemental Figure S6B). Similar results were observed in HeLa cells in which LC3a/b/c or GABARAP/L1/L2 were simultaneously depleted by CRISPR/Cas9 (Vaites *et al.*, 2018) (Supplemental Figure S6K). Owing to functional redundancy, when GABARAP, GABARAP-L1, and GABARAP-L2 were knocked down individually, a statistically significant decrease in accumulation of P23H-R in foci with LAMP was not observed (unpublished data) (Vaites *et al.*, 2018).

To evaluate where in ERAA GABARAP is required for P23H-R degradation, we asked whether GABARAP is present in the ER-connected phagophores proposed to extend into the cytosol from WIPI foci (Figure 6, B and C). Endogenous GABARAP was detected in foci with P23H-R in the ER (Figure 6B). In three-color live-cell imaging, a focus containing P23H-R-eGFP (green), HaloTag-GABARAP (cyan), and WIPI1-mCherry (red) was observed (Figure 6C). In the time course shown at $t = 0$ and $t = 1$ s, signals for P23H-R, GABARAP, and WIPI1 colocalize. At $t = 3$ and 4 s, the colocalized signals for P23H-R and GABARAP have moved away from WIPI but remain attached to the ER, suggesting that GABARAP is present in the membranes of phagophores with WIPI.

In four-color live-cell imaging for cells expressing P23H-R (green), WIPI1-mCherry (red), HaloTag-GABARAP (cyan), and LAMP1-mTagBFP2 (magenta) (Figure 6D), a lysosome (already containing P23H-R) was observed to dock ($t = 20$–40 s) at an ER microdomain containing WIPI1, P23H-R, and GABARAP, followed by the lysosome's departure ($t = 50$ s). The WIPI1 foci remained intact after lysosome departure. These data demonstrate the presence of GABARAP in phagophores with P23H-R and also in lysosomes that contain P23H-R transiently associating with WIPI1 rings.

Docking times between WIPI1 and LAMP1 averaged 22 s (Supplemental Figure S6F) and varied from short interactions (less than 10 s) to associations that lasted up to 70 s (Supplemental Figure S5A). siGABARAP/L1/L2 was not observed to interfere with the WIPI1:lysosome docking nor to change the average docking time of LAMP1 to omegasomes (Supplemental Figure S6F). Therefore,

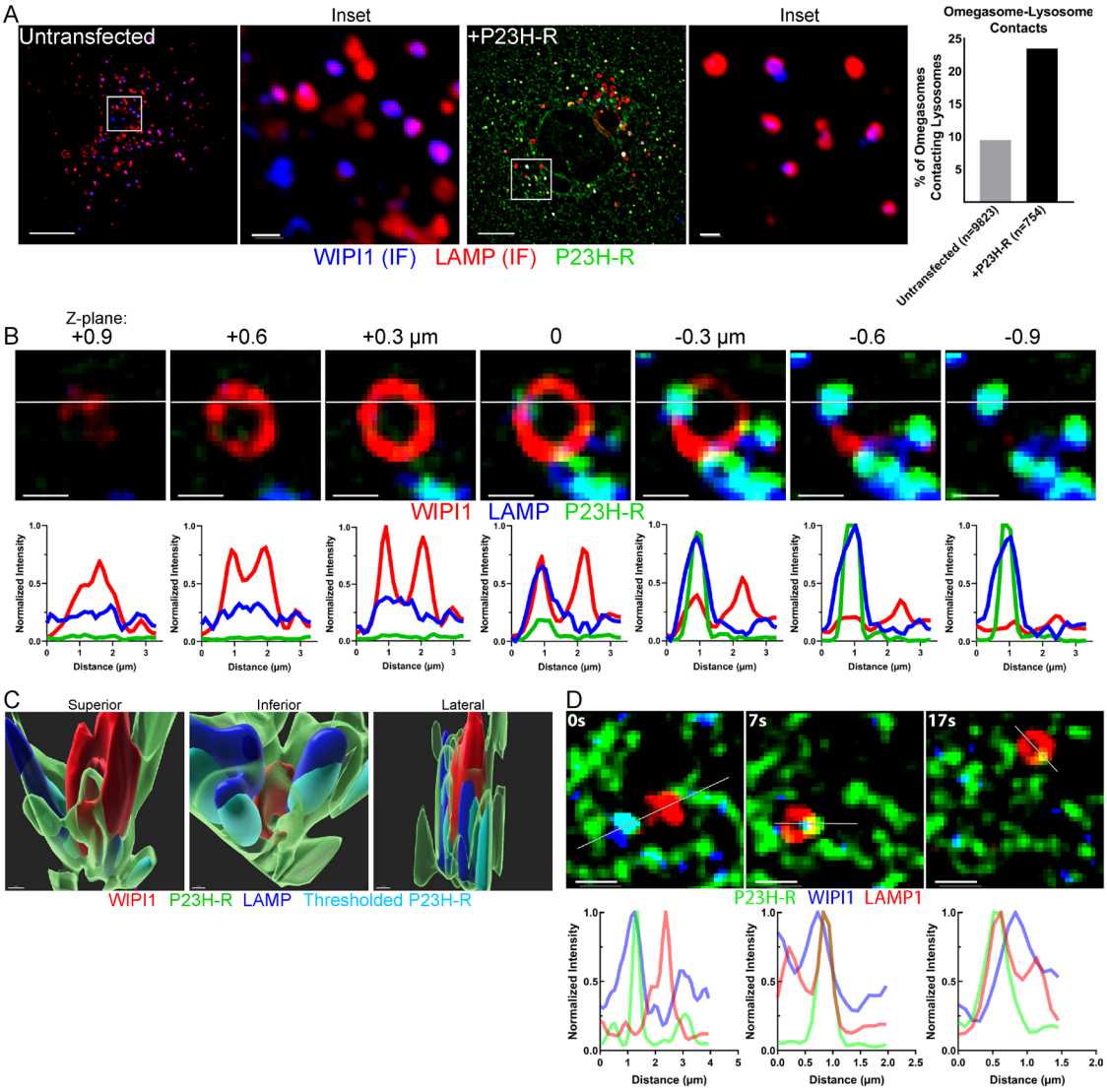

FIGURE 5: Live-cell imaging reveals P23H-rhodopsin transfer to lysosomes occurs at omegasome contacts. (A) Left: Fixed-cell epifluorescence microscopy of COS-7 cells expressing P23H-R (green) with immunofluorescence staining for LAMP1 (red) or WIPI1 (blue). Inset for "+P23H-R" condition shows muted P23H-R channel. Right: Bar graph of LAMP1-WIPI1 contact frequencies seen in each condition from object detection. Scale bars: whole-cell views = 10 µm; insets = 1 µm. Live-cell confocal microscopy with resonant scanning of COS-7 cells expressing P23H-R, WIPI1-mCherry, and mTagBFP2-LAMP1. (B) Slices of *z*-stack with plot profiles of drawn line underneath each respective image. Scale bar = 1 µm. (C) Three-dimensional view of surface renders for the *z*-stack shown in B. "Thresholded P23H-R" refers to similar intensity thresholding (top 10% of histogram intensities) as displayed in blue in B. "P23H-R" in transparent green includes the top 90% of intensities recorded for P23H-R in the *z*-stack. Scale bar = 0.1 µm. (D) *z*-stack time lapse of mTagBFP2-LAMP1 docking and departing from WIPI1-mCherry site containing P23H-R.

docking of lysosomes to WIPI1 foci does not appear to require GABARAP.

A close view of a WIPI1 ring containing a docked lysosome in live siGABARAP/L1/L2 cells shows the presence of P23H-R phagophores extending from the central region of a WIPI1 ring. There is a lysosome docked to the WIPI1-decorated ER surface juxtaposed to the P23H-R–enriched phagophore; however, the docked lysosomes do not contain P23H-R (Figure 6E). This result contrasts with what is observed in normal cells where P23H-R colocalizes with LAMP at the edge of a WIPI1 ring (Figure 5B). Terminal autophagic transfer of P23H-R from phagophores to lysosomes appears to require GABARAP.

To understand why GABARAP/L1/L2, but not LC3a/b/c, depletion, blocks P23H-R exit from omegasomes, we added purified GST-GABARAP and GST-LC3b to HEK293 cell extracts and performed pull downs (Supplemental Figure S6, H and I). GST-GABARAP and GST-LC3b pulled down JB12 and the ER-phagy receptor CCPG1 and TEX264. Remarkably, GST-GABARAP, but not GST-LC3b, pulled down FIP200 and ULK1. The JB12 homologue JB14, which is not required for ERAA, was not present in pull downs. Thus, JB12, FIP200, and ULK1 are present in GABARAP-containing complexes and ULK1 absent for LC3-containing complexes. In addition, FIP200, ULK1, and JB12 coeluted with GABARAP in a pull down of cells expressing 3xFLAG-GABARAP (Supplemental Figure S6J). These data are consistent with previous observations on the specificity of interactions between different GABARAP and LC3 family members with FIP200 and ULK1 (Wirth *et al.*, 2019; Grunwald *et al.*, 2020). Endogenous JB12 and FIP200 colocalize with P23H-R in small foci

within omegasome rings (Figure 4A), and JB12, ULK1, and FIP200 are present in complexes with GABARAP (Supplemental Figure S6, H and J). In addition, we detected GABARAP signals colocalized in the membrane of lysosomes with P23H-R (Supplemental Figure S6A). The collective data presented suggest a model in which JB12 delivers P23H-R to omegasomes and that GABARAP facilitates P23H-R movement from the ER to lysosomes that dock with WIPI1 rings (Figure 7). Additional studies with reconstituted systems are now required to define the detailed molecular mechanisms for JB12 and GABARAP at respective early and late stages of ERAA.

DISCUSSION

P23H-R degradation intermediates accumulate in globally misfolded and kinetically-trapped states that are triaged between ERAD and autophagy via a mechanism involving the ER transmembrane and unfolded protein response regulatory kinase IRE1 (Chiang *et al.*, 2012). Herein, it is reported that cross-talk between the Hsp40/Hsp70 chaperone system and canonical autophagy initiation machinery facilitates P23H-R triage to ERAA (Figure 7). The ER transmembrane JB12 and cytosolic Hsp70 act as substrate selectors for E3 ligases that facilitate ERAD of globally misfolded membrane proteins (Yamamoto *et al.*, 2010; Grove *et al.*, 2011; Sopha *et al.*, 2012; Houck *et al.*, 2014). ERAD-RMPs interact with JB12/Hsp70 complexes for extended time periods, with JB12 being necessary for P23H-R entry into the ERAA pathway. JB12 and FIP200 colocalize with P23H-R in foci on the rim of omegasomal rings. Products of GABARAP pull downs contain JB12, FIP200, and ULK1 (Supplemental Figure S6H). Hsp70 and Hsp90 regulate the activity of kinases that include ULK1, so JB12 and Hsp70 interactions with FIP200 and ULK1 could be of a regulatory nature (Joo *et al.*, 2011). In such a scenario, JB12 would have dual functions: one, as a molecular chaperone that maintains P23H-R in a degradable detergent-soluble state; two, in the focal regulation of ULK1/FIP200 action on ERAD-RMP–containing ER tubules that associate with omegasomes (Figure 7).

Data presented herein on P23H-R and those published on the ERAA client N1303K-CFTR (He, Houck, Kennedy, *et al.*, 2021) suggest that ERAD-RMPs accumulate in complexes with JB12/Hsp70 and ER tubules containing JB12/Hsp70/ERAD-RMP complexes are converted into phagophores via the action of ULK1/FIP200 that localize on WIPI-decorated omegasomes (Proikas-Cezanne *et al.*, 2015; Joachim and Tooze, 2016; Ktistakis and Tooze, 2016). Discrete foci containing JB12, FIP200, and P23H-R or N1303K-CFTR decorate the edge of omegasomes. Data presented herein show P23H-R–containing ER tubules to snake across and through WIPI1-coated ER membranes. ER tubules containing P23H-R that extend into the cytosol from omegasomes are devoid of the ER transmembrane chaperone calnexin as well as JB12. These tubules are decorated with LC3 and GABARAP, which is consistent with them being ER-connected phagophores (Axe *et al.*, 2008; Hayashi-Nishino *et al.*, 2009). The presence of P23H-R within the membranes of ER-connected phagophores is a novel feature of ERAA that is not predicted by models for selective ER-phagy (Ferro-Novick *et al.*, 2021).

A novel feature of ERAA is that the transfer of ERAD-RMPs to lysosomes is associated with lysosome docking to WIPI1 rings. The association of lysosomes with WIPI1 rings occurs over ~10–70 s time spans. In control cells, around 10% of all endogenous WIPI1 foci contain a docked lysosome, and that docking frequency increases 2.5-fold upon P23H-R expression. Docking of lysosomes to WIPI1 rings does not require GABARAP, but the transfer of P23H-R from the ER to lysosomes is GABARAP dependent. Three-dimensional reconstruction of images in *z*-stacks taken in live cells of a WIPI1 ring, P23H-R–containing phagophore, and lysosome shows the extent to which these different structures are in contact. Lysosomes are observed to dock in a notch on the distal end of a WIPI1 ring and are enriched in P23H-R. Signal from ER-localized ERAD-RMPs is contiguous through WIPI1-associated lysosomes, which provides an interface where efficient transfer of P23H-R from the ER to lysosomes can be coupled to docking events.

Lysosomes dynamically interacting with omegasomes that contain P23H-R phagophores was unanticipated. Lysosomes dock with the ER via a mechanism involving the ER-localized protrudin and ORP1L through their recognition of PtdIns3*P* pools present on the surface of lysosomes (Pedersen *et al.*, 2020). If ORP1L and protrudin were present in omegasomes, they could mediate the observed lysosome-omegasome docking. WIPI1 was recently shown to oligomerize and insert its amphipathic helices into tubular membranes of endocytic organelles to drive their fission (De Leo *et al.*, 2021). It is therefore possible that WIPI1 or a different WIPI family member mediates the fission of P23H-phagophore membranes during P23H-autophagosome formation in a process that is coordinated with lysosome docking. Cargo transfer at lysosomes also describes chaperone-mediated autophagy (CMA), a process mediated by the Hsp70 HSPA8, whereby cargo is directly transferred across the lysosome membrane. However, CMA is noted as a VPS34-independent process (Klionsky *et al.*, 2021), which excludes CMA from playing a role in ERAD-RMP degradation as our data show involvement in ERAA of ULK1, Beclin-1, and VPS34 (Supplemental Figure S2).

The ER is constantly challenged with misfolded biogenic intermediates accumulating in both the ER membrane and lumen. It appears that ERAD-resistant degradation intermediates accumulating in the lumen versus the ER membrane are delivered to the lysosome via different routes involving different machinery (Houck *et al.*, 2014; Fregno *et al.*, 2018; Forrester *et al.*, 2019; Ferro-Novick *et al.*, 2021). For example, ERLAD of ERAD-resistant lumenal pools of mutant α-1-antitrypsin occurs via a mechanism involving client selection by a complex containing the ER-phagy receptor FAM134B and the ER transmembrane and lectin binding chaperone calnexin (Fregno *et al.*, 2018). Trafficking of ERAD-resistant α-1-antitrypsin from the ER to lysosome is proposed to occur in single membrane vesicles that are formed via a mechanism that requires the autophagy receptor FAM134B, but not the autophagy initiation kinase ULK1 (Fregno *et al.*, 2018). In contrast, ERAA of ERAD-resistant membrane proteins does not appear to involve FAM134B and is dependent on ULK1 and Beclin1. Data presented herein, and in previous studies, suggest that JB12 interacts with ERAD-RMPs and FIP200/ULK1 to focally regulate flux through the ERAA pathway (Houck *et al.*, 2014; He, Houck, Kennedy, *et al.*, 2021). ERAD-RMPs accumulate in the lysosome membrane and lumen, which is consistent with a double-membrane autophagosome derived from ER-connected phagophores and subsequent delivery of P23H-R to lysosomes. P23H-R present in the outer autophagosomal membrane would accumulate in the lysosome membrane with intermediates present in the inner membrane entering the lumen (Figure 7). These interpretations are consistent with the observation that, when expressed in the same cell, α–1-antitrypsin and ERAD-RMPs accumulate in different lysosomes (Houck *et al.*, 2014).

GABARAP/L1/L2 depletion leads to the arrest of P23H-R autophagic degradation after it has accumulated in phagophores but before P23H-R transfer to adjacent lysosomes. LC3 is therefore able to support entry of P23H-R into phagophores when GABARAP is depleted, but LC3 does not appear to facilitate transfer of P23H-R to lysosomes. A mechanism for GABARAP function in P23H-R transfer from phagophores to lysosomes is suggested

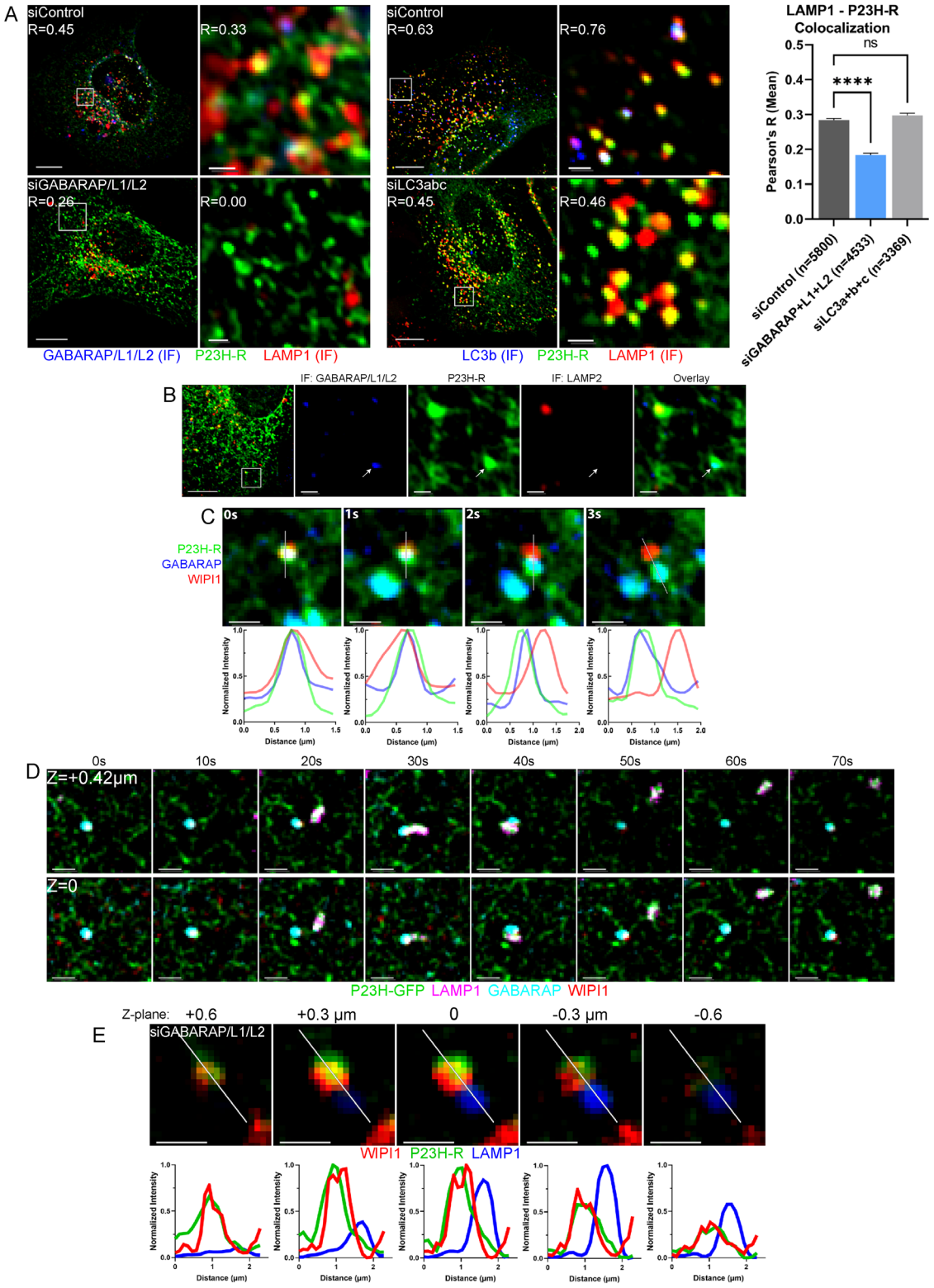

FIGURE 6: P23H-rhodopsin associates with specific autophagic cargo receptors. (A) Left: Fixed-cell epifluorescence microscopy of COS-7 cells expressing P23H-R after siControl, siGABARAP/L1/L2, or siLC3abc knockdown. Right: Bar graph of mean Pearson's *R* values between rhodopsin and LAMP1 calculated within the identified LAMP1 objects. Kruskal–Wallis and Dunn's multiple comparisons tests. (B) Fixed-cell epifluorescence microscopy of COS-7 cells expressing P23H-R and immunolabeled for LAMP2a and GABARAP/L1/L2. (C) Time lapse from live-cell confocal microscopy with resonant scanning of COS-7 cells expressing P23H-R, WIPI1-mCherry, and HaloTag-GABARAP and incubated with 50 nM Janelia Fluor 646 HaloTag Ligand for 30 min before imaging. (D) Same as in C but also expressing mTagBFP2-LAMP1. Manual *x*-offset correction for P23H-R and HaloTag-GABARAP = +11 pixels. (E) Live-cell confocal microscopy with resonant scanning of COS-7 cells expressing P23H-R,

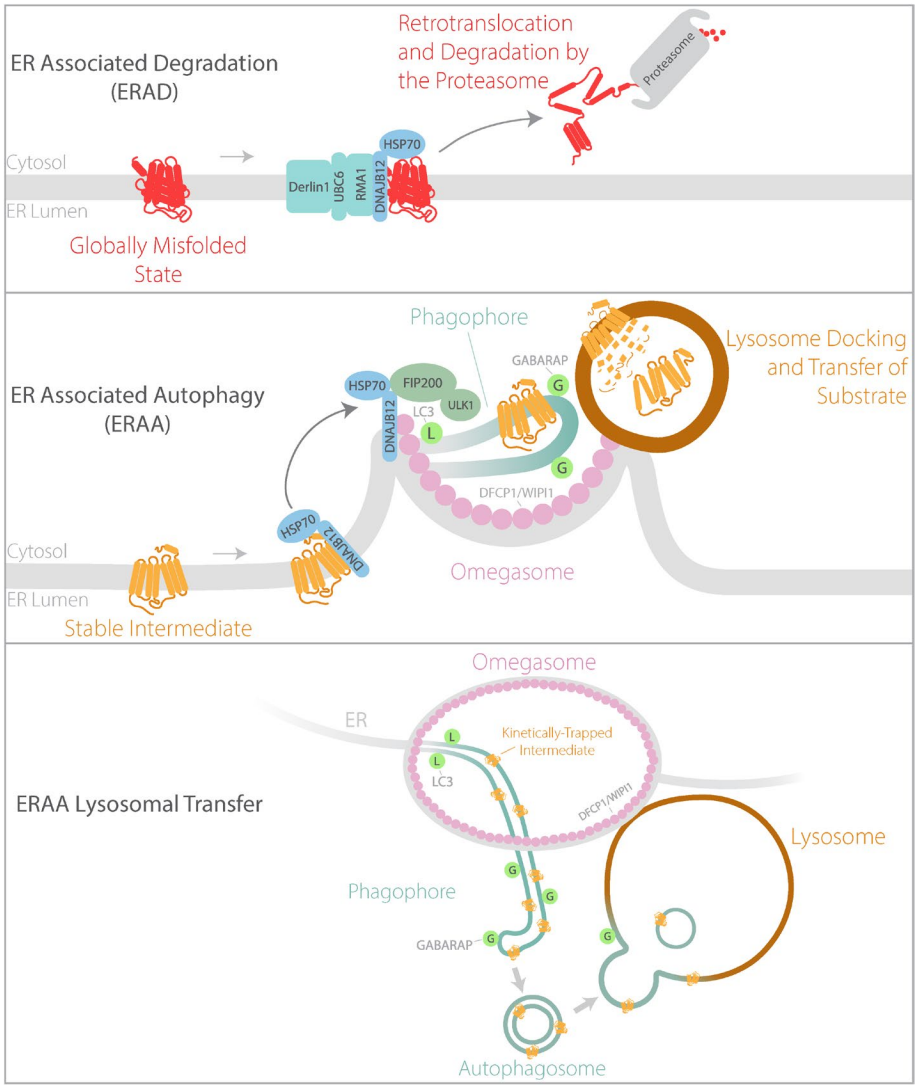

FIGURE 7: Model for the degradation of misfolded membrane proteins by ER-associated autophagy. Illustration of the model describing the triage of ERAD-resistant membrane proteins to lysosomes.

by the observation that GABARAP, FIP200, and ULK1 are present in the same complexes. The GABARAP present in omegasomes could therefore mediate localization of ULK1 to locations where its action is required to induce liberation of autophagosomes containing P23H-R. Such a regulatory mechanism would enable a two-step protection of the ER from toxic misfolded membrane proteins. In step 1, sequestration of P23H-R into phagophores occurs to insulate a dominantly toxic P23H-R intermediate away from other ER components. Step 2 would involve the transfer of P23H-R out of the ER in reactions catalyzed by GABARAP that are coordinated with lysosome docking to WIPI1 rings.

The triage of biochemically stable intermediates of P23H-R to ERAA identifies a cellular mechanism to prevent ERAD-RMPs from saturating JB12 and causing ER stress–induced apoptosis (Sopha *et al.*, 2017). JB12 functions with the E3-ubiquitin ligase GP78 to facilitate the constitutive degradation of the short-lived and ER-associated BCL-2 homologue BOK (Llambi *et al.*, 2016; Sopha *et al.*, 2017). ER stress–dependent degradation of JB12 causes BOK accumulation and primes cells for apoptosis (Sopha *et al.*, 2017). Data presented, and those from related studies, suggest that JB12 and Hsp70 maintain ERAD-RMPs in a detergent-soluble and nonaggregated state that is mobile in the ER membrane (He, Houck, Kennedy, *et al.*, 2021). JB12 is not stress inducible, so cells clear ERAD-RMPs from JB12 via ERAA. JB12 appears to sense ERAD-RMP accumulation and work with Hsp70 to facilitate the focal activation of ERAA by associating with complexes containing FIP200 in omegasomes. This mechanism is proposed to prevent JB12 from entering dead-end complexes with ERAD-RMPs to suppress induction of ER stress–induced apoptosis.

The observation of P23H-R accumulation in lysosome membranes was unexpected. This membrane-localized signal was stronger than that observed in the lumen, even after inhibiting degradation by BafA1, suggesting that the turnover of ERAA substrates within lysosome membranes occurs at a slower rate than that of internalized clients. This may provide a possible explanation for the toxicity of P23H-R in retinitis pigmentosa: cells are able to avoid direct misfolding-related harm through successful triage by ERAA; however, turnover at the endpoint, the lysosome membrane, becomes the limiting factor resulting in lysosome-related toxicity. The possible mechanism for degradation of ERAA clients in the lysosomal membrane could utilize the same method as used to turn over LAMP and other lysosome membrane proteins (Cuervo and Dice, 2000). Alternatively, the cell might rely on lysophagy for degradation of these altered lysosomes (Papadopoulos and Meyer, 2017; Radulovic *et al.*, 2018).

MATERIALS AND METHODS

Reagents, plasmids, and antibodies

The DC Protein Assay (500-0119) and Clarity Western ECL Substrate (170-5061) were from BioRad. The Effectene Transfection Reagent (301427) was from Qiagen. The Lipofectamine RNAiMAX Reagent (100014472) was from Thermo Fisher Scientific. ProLong Diamond antifade mountant without (P36970) or with (P36971) DAPI (4′,6-diamidino-2-phenylindole) was from Thermo Fisher Scientific. BafA1 (11038) and MRT68921 (1990520000040) were from Cayman Chem. PIK-III was from Selleckchem (S7683). Bort (B-1408) was from LC Laboratories. Janelia Fluor 646 HaloTag Ligand (GA1120) was from Promega.

WIPI1-mCherry, and mTagBFP2-LAMP1. Slices of *z*-stack with plot profiles of drawn line underneath each respective image. Scale bar = 1 µm. "GABARAP/L1/L2" includes GABARAP, GABARAP-L1, and GABARAP-L2 concurrently; "LC3abc" includes LC3a, LC3b, and LC3c concurrently. ****$P < 0.0001$. Scale bars: whole-cell views = 10 µm; insets = 1. µm.

Plasmid name	From	Addgene #
lentiCRISPRv2	Feng Zhang, Broad Institute	52961
FLAG-QPD-DNAJB12	This paper	
K46I-ULK1	This paper	
FLAG-DNAJB12	This paper	
S15A-Beclin1	This paper	
GST-GABARAP	This paper	
GST-LC3b	This paper	
WIPI1-mCherry	This paper	
mTagBFP2-Lysosomes-20	Michael Davidson, The Florida State University	55308
HaloTag-GABARAP	This paper	
Rhodopsin-eGFP	Michael Cheetham, University College of London	
P23H-Rhodopsin-eGFP	Michael Cheetham	
pCMV 3xFLAG-GABARAP WT	Robin Ketteler, University College of London	123097
pCMV 3xFLAG-GABARAPL1 WT	Robin Ketteler	123100
pCMV 3xFLAG-GABARAPL2 WT	Robin Ketteler	123103
mCherry-DFCP1	Do-Hyung Kim, University of Minnesota	86746

TABLE 1: Plasmids.

Plasmids used and sources are given in Table 1. Antibodies used along with hosts and manufacturers appear in Table 2.

CRISPR/Cas9 knockout cell line

DNAJB12-KO, FAM134B-KO, or "CRISPR-control" (vector with no insert) HeLa cell lines were generated by lentiviral transduction using the lentiCRISPRv2 plasmid (a gift from Feng Zhang, Broad Institute; Addgene plasmid #52961). Cells were selected with 3 μg/ml puromycin until complete uninfected cell death occurred and then maintained at 0.5 μg/ml during passaging (puromycin removed from media before being used in assays).

CRISPR/Cas9 sequences and targets are shown in Table 3.

Cell culture and transfection

African green monkey kidney cells (COS-7 ATCC CRL-1651), human embryonic kidney cells (HEK293, ATCC CRL-1573), and human cervix epithelial cells (HeLa cells ATCC-CCL2) were cultured in DMEM supplemented with 10% fetal bovine serum (Sigma-Aldrich, St. Louis, MO) and 10 U/ml penicillin, 10 μg/ml streptomycin (GIBCO, Carlsbad, CA) at 37°C, 5% CO_2.

Plasmid transfections in cell lines were performed using Effectene Transfection Reagent following the product instruction. For knockdown experiments, all siRNAs were purchased from Thermo Fisher Scientific. siRNA sequences and targets are given in Table 4. For some target genes, two siRNAs to the same target gene were used to increase knockdown efficiency. COS-7 or HEK293 cells that were seeded into a six-well plate at 3×10^5 cells/well for 20 h were transfected at 5 picomoles per well of siRNA with Lipofectamine RNAiMAX. Twenty hours posttransfection, the cells were split again to the appropriate density for transfection of plasmids using Effectene Transfection Reagent. The following drug treatments were used at these concentrations for 6 h unless otherwise indicated: 100 nM BafA1; 10 μM Bort, 10 μM 9CR.

Protein sample preparation for SDS–PAGE and western blotting

COS-7 or HEK293 cells were harvested from plates with citric saline (135 mM KCl, 15 mM sodium citrate). Cell pellets were washed in phosphate-buffered saline (PBS) and then resuspended in PBST lysis solution (1% [vol/vol] Triton X-100 in PBS) supplemented with 1 mM PMSF (phenylmethylsulfonyl fluoride), 1× complete protease inhibitor cocktail (Roche, Basel, Switzerland). Laemmli sample buffer (2×) without reducing agent was added, and the total lysates were homogenized by sonication. Protein concentrations were measured using detergent-compatible DC Protein Assay Reagent, and 50 mM dithiothreitol (DTT) was added before samples were resolved by SDS–PAGE and western blot analysis. Protein signal was detected by Clarity western ECL substrate and visualized by LAS680 imager (GE Life Sciences, Pittsburgh, PA). Images were analyzed by ImageJ (National Institutes of Health, USA) and quantified with ImageQuant (GE Life Sciences, Pittsburgh, PA).

Coimmunoprecipitation assay

HEK293 or COS-7 cell lysates in PBST solution (1% Triton X-100 in PBS) were centrifuged at 100,000 × *g* at 4°C for 10 min to remove any insoluble fraction. Protein concentrations were measured using the DC Protein Assay, and samples of equal amounts of proteins were used for immunoprecipitation analysis. To conduct pull downs, the indicated antibodies cross-linked to protein G agarose beads (Invitrogen) were incubated with cleared lysate for 1 h at 4°C. Beads were washed 3× with PBST lysis buffer. Bound proteins were eluted from beads via incubation with 2× SDS–PAGE sample buffer without reducing agent at 37°C for 15 min. Anti-FLAG M2 beads (Sigma-Aldrich, St. Louis, MO) were used to pull down proteins interacting with FLAG-tagged proteins. After washing, proteins bound were eluted with FLAG peptide. Eluted proteins were subjected to SDS–PAGE and western blot analysis as described above.

qPCR

The qPCR (quantitative polymerase chain reaction) primers are given in Table 5. HeLa cell pellets were subjected to RNA isolation using the RNeasy Mini Kit (Qiagen #74106) according to the manufacturer's instructions. The resulting RNA was treated with the TURBO DNA-*free* Kit (Invitrogen; #AM1907) and subsequent reverse transcription using SuperScript IV VILO Master Mix (Invitrogen; #11756050) according to the manufacturer's instructions. The qPCRs

Antibody target/name	Host	Catalogue #	Manufacturer
Anti-mouse IgG (H+L) secondary antibody, horseradish peroxidase (HRP)	Goat	31430	Thermo Fisher Scientific
Anti-rabbit IgG F(ab')2 secondary antibody, HRP	Goat	31461	Thermo Fisher Scientific
Anti-mouse IgG (H+L) highly cross-adsorbed secondary antibody, Alexa Fluor 488	Goat	A11029	Thermo Fisher Scientific
Anti-mouse IgG (H+L) cross-adsorbed secondary antibody, Texas Red-X	Goat	T-862	Thermo Fisher Scientific
Anti-rabbit IgG (H+L) cross-adsorbed secondary antibody, Texas Red	Goat	T-2767	Thermo Fisher Scientific
Anti-mouse IgG (H+L) highly cross-adsorbed secondary antibody, Alexa Fluor Plus 647	Goat	A32728	Thermo Fisher Scientific
Anti-rabbit IgG (H+L) highly cross-adsorbed secondary antibody, Alexa Fluor Plus 647	Goat	A32733	Thermo Fisher Scientific
Anti-mouse IgG (H+L) highly cross-adsorbed secondary antibody, Alexa Fluor Plus 594	Goat	A32742	Thermo Fisher Scientific
Anti-rabbit IgG (H+L) highly cross-adsorbed secondary antibody, Alexa Fluor Plus 594	Goat	A32740	Thermo Fisher Scientific
Anti-rabbit IgG (H+L) cross-adsorbed secondary antibody, Alexa Fluor 405	Goat	A31556	Thermo Fisher Scientific
FAM134B	Rabbit	NBP2-55248	Novus Biologicicals
Sec62	Rabbit	NBP1-84045	Novus Biologicicals
Calnexin	Rabbit	C4731	Sigma-Aldrich
GABARAP/L1/L2	Rabbit	ab109364	Abcam
LC3b	Rabbit	L7543	Sigma
DNAJB12	Rabbit	16780-1-Ap	Proteintech
DNAJB14	Rabbit	16501-1-AP	Proteintech
TEX264	Rabbit	25858-1-AP	Proteintech
ULK1	Rabbit	4773	Cell Signaling Technology
CCPG1	Rabbit	13861-1-AP	Proteintech
FIP200	Rabbit	10043-2-AP	Proteintech
eIF2a	Rabbit	3597	Cell Signaling Technology
P-eIF2a	Rabbit	9722	Cell Signaling Technology
GFP	Mouse	11814460001	Roche
Beclin	Rabbit	3738	Cell Signaling Technology
Calnexin	Rabbit	C4731	Sigma
ATL3	Mouse	Custom	Craig Blackstone, National Institutes of Health
WIPI	Rabbit	PA5-34452	Thermo Fisher Scientific
Tubulin	Mouse	T4026	Sigma
GAPDH	Mouse	60004-1-Ig	Proteintech
Bip	Rabbit	3183	Cell Signaling Technology
HSP70	Rabbit	SPA-757	Assay Designs
SQSTM1 (P62)	Mouse	H00008878-M01	Abnova
LAMP-2(α)	Mouse	555803	BD Pharmingen
LAMP1	Mouse	H4A3	Developmental Studies Hybridoma Bank
VPS34	Rabbit	4263S	Cell Signaling Technology
BiP	Rabbit	3183	Cell Signaling Technology
GFP (EM)	Rabbit	ad6556	abcam
FLAG	Mouse	F1804	Sigma
GFP (Westerns)	Mouse	11814460001	Roche
HSP70	Rabbit	SPA-757	Assay Designs
GST	Mouse	A00865	GenScript

TABLE 2: Antibodies.

Target	Name	Sequence
DNAJB12	DNAJB12 Human_guideRNA615revU6sensepX330	CACCGGCTCTTGTCATCGCCGAAC
DNAJB12	DNAJB12 Human_guideRNA615revU6antisensepX330	AAACGTTCGGCGATGACAAGAGCC
DNAJB12	DNAJB12 Human_guideRNA223revU6sensepX330	CACCGTCAATCAGGGCGCGAACTCG
DNAJB12	DNAJB12 Human_guideRNA223revU6antisensepX330	AAACCGAGTTCGCGCCCTGATTGAC
FAM134B	FAM134B_guideRNA220revU6sensepX330	CACCGAGATAGCTGAGTATAACCCC
FAM134B	FAM134B_guideRNA220revU6antisensepX330	AAACGGGGTTATACTCAGCTATCTC
FAM134B	FAM134B_guideRNA445revU6sensepX330	CACCGCAACCGTGAGGCTAATCTT
FAM134B	FAM134B_guideRNA445revU6antisensepX330	AAACAAGATTAGCCTCACGGTTGC

TABLE 3: CRISPR/Cas9 sequences.

Target	Catalogue #	Sense	Antisense
FAM134B	s29012	GCAGAAUCAUGGAUGAAUUTT	AAUUCAUCCAUGAUUCUGCAA
FAM134B	s29013	GAGGUAUCCUGGACUGAUATT	UAUCAGUCCAGGAUACCUCTG
TEX264	s28030	GAGUGACACGAGUUCUGUATT	UACAGAACUCGUGUCACUCAT
TEX264	s28031	CUCCAUCGCUGUCUACUAUTT	AUAGUAGACAGCGAUGGAGCG
CCPG1	s17661	GGAAGAGUUAAACAAACUATT	UAGUUUGUUUAACUCUUUCCTG
CCPG1	s17659	CAGUUUUUAGUUGACUAUUUTT	AAAUAGUCACUAAAAACUGTT
DNAJB12	s29440	GCGGCUUCCCUUCUAGUAATT	UUACUAGAAGGGAAGCCGCCG
DNAJB12	S29438	CGCUAUACCUACCAGCAAATTT	UUUGCUGGUAGGUAUAGCGCA
DFCP1	s28712	GGAUGGGUCUCGCAAAAUATT	UAUUUUGCGAGACCCAUCCAG
SEC62	s14188	GGGAGUCUGUGGUUGACUATT	UAGUCAACCACAGACUCCCTG
SEC62	s14190	GGACCAAAAGCAGACUUAATT	UUAAGUCUGCUUUUGGUCCTT
ATL3	s24755	GGCUUCUUCUCAUAUCGGUTT	ACCGAUAUGAGAAGAAGCCTG
ATL3	s24754	CCCUUAUGAAUAUAGCUAUTT	AUAGCUAUAUUCAUAAGGGAA
GABARAP	s22361	GAAGACUUCUUUCUCUACATT	UGUAGAGAAAGAAGUCUUCTT
GABARAPL1	s24331	UGAGGACAAUCAUGAGGAATT	UUCCUCAUGAUUGUCCUCATA
GABARAPL2	s22385	CAGCUUUACGAGAAGGAAATT	UUUCCUUCUCGUAAAGCUGTC
LC3B	s224886	CCUUCGAACAAAGAGUAGATT	UCUACUCUUUGUUCGAAGGTG
LC3B2	s196888	AGUUCAUCUAAUCACAGAUTT	AUCUGUGAUUAGAUGAACUGA
LC3C	s54188	ACUUGCUGGUGAACAACAATT	UUGUUGUUCACCAGCAAGUAA
LC3A	s39155	UGAGCGAGUUGGUCAAGAUTT	AUCUUGACCAACUCGCUCATG

TABLE 4: siRNA sequences.

Gene	Forward sequence (5′–3′)	Reverse sequence (5′–3′)
HSPA5	GCTATACCTACCAGCAAAGG	GACACGAGAATCAGGATGAG
eIF2B1	CAGCAAGACGTCCCAGATAAG	CAGCAGAGTGATTAAGGAAGGG
HERPUD1	TGCTGGTTCTAATCGGGGACA	CCAGGGGAAGAAAGGTTCCG
SYVN1	CCTCAAACACCAGTTCTACC	GGAGGAAGACAAGGACAAAG
HSPA1A	TGGTGCTGACCAAGATGAAG	GCTGCGAGTCGTTGAAGTA
HSPA8	AACTGCTGGTGGAGTAATG	GGCTGGTTGTCAGAATAGG
TUBB	CAGCAAGATCCGAGAAGAG	GAGAGGGTGGCATTGTAG

TABLE 5: Quantitative PCR (qPCR) primers.

were prepared in MicroAmp Fast Optical 96-Well Reaction Plates (Applied Biosystems; #4346906) using PowerUp SYBR Green Master Mix (Applied Biosystems; #A25742) and then briefly spun down before being run in the QuantStudio 3 Real-Time PCR Instrument 96-Well 0.1 ml Block (Applied Biosystems; #A28131). Relative gene expression was quantified by the ΔΔCT method within QuantStudio 3 software (Applied Biosystems). Quantitation is relative to untransfected cells using *TUBB* as the reference gene.

Triton X-100 solubility assay

Harvested cell pellets were lysed in PBST (1% Triton X-100 in PBS) and separated into soluble and insoluble fractions by centrifugation at 20,000 × *g* for 30 min at 4°C. The insoluble fraction was resuspended in a 2× sample buffer with an equal volume of soluble fraction and sonicated. Total lysates, soluble fractions, and insoluble fractions were resolved with SDS–PAGE and subjected to western blot analysis.

Immunofluorescence microscopy

COS-7 or HeLa cells were grown on #1.5 coverslips (Thermo Fisher Scientific; 12541A) in six-well plates. After transfection and treatment, conditions with HaloTag fusion protein expression were also incubated with 100 nM Janelia Fluor 646 HaloTag Ligand (Promega; GA11220) for 30 min before fixation. Cells were fixed at –20°C for 5 min with precooled methanol. Cells were rehydrated by being washed 3× in PBS and blocked with 3% bovine serum albumin (BSA) in PBS for 30 min before immunostaining with various antibodies in 3% BSA in PBS for 1 h. Goat anti-mouse or goat anti-rabbit secondary antibodies with different fluorophores were used to detect proteins of interest in 3% BSA in PBS for 20 min. Coverslips were washed 8× with PBS, mounted onto slides using ProLong Diamond antifade mountant without (P36970) or with (P36971) DAPI (Invitrogen), and then sealed with nail polish. Slides were allowed to dry in the dark at room temperature for at least 12 h before imaging.

Fixed-cell image acquisition

Epifluorescent images were acquired with an Olympus ix-81 motorized inverted microscope with CellSens acquisition software v1.0 (Olympus, Center Valley, PA), with a manual Olympus stage and software-based *z*-step, using an X-Cite 120LED Boost High-Power LED illumination System (Excelitas Technologies, Waltham, MA). Excitation/emission wavelengths were controlled using Lambda 10-3 Optical Filter Changer (Sutter Instrument, Novato, CA) equipped with the following filter excitation wheels located at the light source: AT350/50x, ET402/15x, ET490/20x, ET555/25x, ET645/30x (Chroma, Bellows Falls, VT). The emission wheel located on the camera port contained the following: ET455/50m, ET525/36m, ET605/52m, ET705/72m (Chroma). Between both wheels contained the 89100bs dichroic (Chroma). An Olympus UPlanFL N 60x/1.25 Oil Iris objective lens was used for acquisition. Detector used was an ORCA-Flash4.0 V3 Digital CMOS camera (Hamamatsu, Hamamatsu City, Japan); 2 × 2 binning, 6.5μmx6.5μm pixel size, 2048 × 2048 chip size, with rolling shutter. Confocal images were captured on an LSM 880 with Airyscan with ZEN acquisition software (Zeiss, Jena, Germany). *z*-stacks were acquired and processed using the Airyscan Processing algorithm included in ZEN.

Live-cell imaging

COS-7 cells were cultured in 35 mm glass-bottom dishes (MatTek; P35G-1.5-10-C). After overnight transfection with fluorescent-tagged proteins, cells were rinsed with prewarmed FluorBrite DMEM (Life Technologies) and kept in the same medium during drug treatment and imaging. Live-cell imaging was carried out using LSM 880 with Airyscan and live-cell incubation chamber (Zeiss, Jena, Germany) where indicated. For all others images were acquired by an inverted Olympus FV3000RS confocal laser point-scanning microscope (Olympus Corporation, Tokyo, Japan) equipped with four GaAsP detectors, resonant and galvanometer scanners attached to a fully motorized Olympus IX83 inverted stand equipped with an Olympus IX3-SSU motorized scanning stage encoded with an ultrasonic motor in the UNC Neuroscience Microscopy Core (RRID:SCR_019060), equipped with a Tokai Hit stage-top incubation chamber (model STXG-WSKMX-SET) at 37°C with 5% CO_2 and humidity using a 60×/1.4NA PLAPON oil immersion (Olympus) objective lens. A 405 nm, 50 mW diode laser was used for excitation of Alexa Fluor 405, a 488 nm, 20 mW diode laser was used for excitation of mEGFP, a 561 nm diode, 20 mW laser was used for excitation of Alexa Fluor 568, and a 640 nm, 40 mW diode laser was used for excitation of Alexa Fluor 647. A 405/488/561/640 dichroic mirror was used to acquire all channels. Laser power was adjusted between cells to maintain similar fluorescence intensity histograms between cells, with final transmittance of laser power set in the software ranging from 1.0 to 8.5%, with a 10% ND filter in the light path. All images were acquired in resonance scanning mode, at 16 bit depth, with channels acquired sequentially by line on GaAsP detectors, using 10× frame averaging with a pinhole size of 217 μm, a zoom of 4.62×, a frame size of 512 × 512 pixels with pixel sizes of 0.090 μm, and a *z*-step of 0.42 μm between slices. Light emitted from the Alexa Fluor 405 channel was collected in the detector unit HSD1 (GaAsP detector) with a variable-bandpass filter range of 409–484 nm and voltage (HV) set to 500 V. Light emitted from the mEGFP channel was collected in the detector unit HSD3 (GaAsP detector) with a variable-bandpass filter range of 492–557 nm and voltage (HV) set to 500 V. Light emitted from the Alexa Fluor 568 channel was collected in the detector unit HSD2 (GaAsP detector) with a variable-bandpass filter range of 575–638 nm and voltage (HV) set to 650 V. Light emitted from the Alexa Fluor 647 channel was collected in the detector unit HSD4 (GaAsP detector) with a variable-bandpass filter range of 646–746 nm and voltage (HV) set to 480 V. Images were acquired and deconvoluted using CellSens software (Olympus) and processed with Bioimage ICY (de Chaumont *et al.*, 2012) and Adobe Photoshop.

Image quantitation and processing

Images were deconvoluted using the v3.2 CellSens constrained iterative Advance Maximum Likelihood algorithm with five iterations using GPU acceleration and then processed with Bioimage ICY v2.4.0.0. All views of microscopy images with scale bars were made using Bioimage ICY (v2.2.1.0) (de Chaumont *et al.*, 2012) with the "Scale Bar" (Thomas Provoost, Pasteur Institute; http://icy.bioimageanalysis.org/plugin/scale-bar/) (v3.2.0.0) plug-in. Signal profiles of images were generated using a line region of interest (ROI) drawn in Bioimage ICY and then "Plot Profile" was run using the built-in ImageJ within ICY. Profiles were normalized to the maximum intensity. For live-cell plot profiles, the lowest intensity was subtracted within each channel and then the profile was normalized to the maximum intensity.

Statistical analysis of signal colocalization was achieved through the calculation of Pearson's correlation coefficients (*R*). For images with an *R* value inscribed in the image, an ROI was manually drawn and cropped around the cell of interest or inset, followed by extraction of the in-focus plane using Bioimage ICY. The "Coloc 2" plug-in for FIJI/ImageJ was then used to calculate Pearson's correlation coefficients between eGFP-rhodopsin and different sets of markers (Schindelin *et al.*, 2012). For images where Pearson's *R* was calculated within identified objects, a custom CellProfiler

(v3.1.9; Broad Institute, Cambridge, MA) (McQuin *et al.*, 2018) pipeline was developed to identify LAMP1 objects within cells expressing rhodopsin by thresholding the rhodopsin channel and then masking the LAMP1 channel. Next, "IdentifyPrimaryObjects" was used to identify LAMP vesicles with manual global thresholding used, and the "shape" parameter was used to distinguish clumped objects. These identified LAMP1 objects were then used to calculate Pearson's *R* within each object for a given marker. To measure instances of WIPI1-LAMP docking, the same pipeline was used for both LAMP and WIPI1 object identification, then WIPI1 objects masked by LAMP objects, and then remaining foci counted to identify docking events. Frequency was calculated by dividing the number of LAMP1-masked omegasome objects by the total number of omegasomes identified. Statistical analysis and plot generation were performed in Prism GraphPad 9 (San Diego, CA).

GST-GABARAP and GST-LC3 purification

GST-GABARAP was expressed in *Escherichia coli* strain BL21(DE3) and purified as follows: pellets from 300 ml of culture were harvested after a 3 h induction with 0.2 mM IPTG (isopropyl β-D-1-thiogalactopyranoside) and lysed by sonication in buffer PBS (140 mM NaCl, 2.7 mM KCl, 10 mM Na_2HPO_4, 1.8 mM KH_2PO_4, pH 7.4), 2 mM DTT, and 0.1 mM PMSF. The high-speed supernatant was loaded onto a GSTrap 4B column equilibrated with PBS. Bound GST-GABARAP was eluted by 50 mM Tris-HCl, 20 mM reduced glutathione, pH 8.0. Final eluate was dialyzed against 20 mM HEPES, pH 7.4, 150 mM NaCl, 2 mM DTT, 0.1 mM PMSF. Aliquots of protein were frozen in liquid nitrogen and store at –80°C until used.

GST-GABARAP and GST-LC3 pull-down assays

HEK293 cells were lysed at 4°C in PBS buffer, 1% Triton X-100, Protease Inhibitor Mixture Tablets Complete (Roche Applied Science), and 1 mM PMSF. High-speed supernatant was incubated with GST-GABARAP or GST-LC3 for 30 min at 4°C and then Glutathione Sepharose (GE 17-5132-01) was added for 30 min at 4°C. After being washed with lysis buffer, the samples were eluted with 2× SDS sample buffer (100 mM Tris-HCl, pH 6.8, 4% SDS, 0.05% bromophenol blue, and 20% glycerol).

Electron microscopy

Cells were harvested 24 h posttransfection with 0.05% trypsin-EDTA (Life Technologies) from a six-well plate and reseeded on Nunc Permanox chamberslides. Cells were allowed to grow for another 24 h and then were fixed with 2% paraformaldehyde/0.5% glutaraldehyde in 0.15 M sodium phosphate buffer, pH 7.4, for 1 h. Following free aldehyde inactivation with 0.2 M glycine in 0.15 M sodium phosphate buffer (PB), cells were permeabilized with 0.1% saponin in PB for 1 h and incubated in a 1:100 dilution of rabbit anti-GFP (Cell Signaling Technology; #2956) overnight at 4°C. After buffer washes, samples were incubated in secondary antibody, 1:100 goat anti-rabbit immunoglobulin G (IgG), 0.8 nm immunogold (Aurion, Electron Microscopy Sciences), for 16 h at 4°C. The cells were postfixed in 2% glutaraldehyde in PB and silver enhanced for 90 min using an Aurion R-Gent SE-EM Silver Enhancement Kit. The monolayers were postfixed in 0.1% osmium tetroxide, dehydrated in ethanol, and embedded in Polybed 812 epoxy resin (Polysciences, Warrington, PA). Ultrathin sections (80 nm) were cut, mounted on copper grids, and poststained with 4% uranyl acetate and lead citrate. Sections were observed using a JEOL JEM 1230 transmission electron microscope (JEOL USA, Peabody, MA) operating at 80 kV, and images were taken using a Gatan Orius SC1000 CCD camera with Digital Micrograph 3.11.0 (Gatan, Pleasanton, CA).

ACKNOWLEDGMENTS

This work was supported by a grant from the National Institutes of Health (GM056981). The University of North Carolina (UNC) Hooker and Neuroscience Imaging Cores housed the Zeiss LSM 880 or Olympus FV3000RS microscopes respectively. Michael Cheetham (University College of London, England) kindly provided the rhodopsin expression plasmids. Transmission electron microscopy was performed at the UNC Department of Pathology Microscopy core. Wade Harper, Harvard Medical School, kindly provided the ATG8 knockout cell lines.

REFERENCES

Boldface names denote co–first authors.

An H, Ordureau A, Paulo JA, Shoemaker CJ, Denic V, Harper JW (2019). TEX264 is an endoplasmic reticulum-resident ATG8-interacting protein critical for ER remodeling during nutrient stress. Mol Cell 74, 891–908.e810.

Athanasiou D, Aguila M, Bellingham J, Li W, McCulley C, Reeves PJ, Cheetham ME (2018). The molecular and cellular basis of rhodopsin retinitis pigmentosa reveals potential strategies for therapy. Prog Retin Eye Res 62, 1–23.

Axe EL, Walker SA, Manifava M, Chandra P, Roderick HL, Habermann A, Griffiths G, Ktistakis NT (2008). Autophagosome formation from membrane compartments enriched in phosphatidylinositol 3-phosphate and dynamically connected to the endoplasmic reticulum. J Cell Biol 182, 685–701.

Bhaskara RM, Grumati P, Garcia-Pardo J, Kalayil S, Covarrubias-Pinto A, Chen W, Kudryashev M, Dikic I, Hummer G (2019). Curvature induction and membrane remodeling by FAM134B reticulon homology domain assist selective ER-phagy. Nat Commun 10, 2370.

Buchberger A (2014). ERQC autophagy: yet another way to die. Mol Cell 54, 3–4.

Chapple JP, Cheetham ME (2003). The chaperone environment at the cytoplasmic face of the endoplasmic reticulum can modulate rhodopsin processing and inclusion formation. J Biol Chem 278, 19087–19094.

Chen Q, Xiao Y, Chai P, Zheng P, Teng J, Chen J (2019). ATL3 is a tubular ER-phagy receptor for GABARAP-mediated selective autophagy. Curr Biol 29, 846–855.e846.

Chen Y, Jastrzebska B, Cao P, Zhang J, Wang B, Sun W, Yuan Y, Feng Z, Palczewski K (2014). Inherent instability of the retinitis pigmentosa P23H mutant opsin. J Biol Chem 289, 9288–9303.

Chiang WC, Messah C, Lin JH (2012). IRE1 directs proteasomal and lysosomal degradation of misfolded rhodopsin. Mol Biol Cell 23, 758–770.

Chino H, Hatta T, Natsume T, Mizushima N (2019). Intrinsically disordered protein TEX264 mediates ER-phagy. Mol Cell 74, 909–921.e906.

Chino H, Mizushima N (2020). ER-phagy: quality control and turnover of endoplasmic reticulum. Trends Cell Biol 30, 384–398.

Conn PM, Ulloa-Aguirre A, Ito J, Janovick JA (2007). G protein-coupled receptor trafficking in health and disease: lessons learned to prepare for therapeutic mutant rescue in vivo. Pharmacol Rev 59, 225–250.

Cuervo AM, Dice JF (2000). Regulation of lamp2a levels in the lysosomal membrane. Traffic 1, 570–583.

de Chaumont F, Dallongeville S, Chenouard N, Herve N, Pop S, Provoost T, Meas-Yedid V, Pankajakshan P, Lecomte T, Le Montagner Y, *et al.* (2012). Icy: an open bioimage informatics platform for extended reproducible research. Nat Methods 9, 690–696.

De Leo MG, Berger P, Mayer A (2021). WIPI1 promotes fission of endosomal transport carriers and formation of autophagosomes through distinct mechanisms. Autophagy 17, 3644–3670.

Delorme-Axford E, Popelka H, Klionsky DJ (2019). TEX264 is a major receptor for mammalian reticulophagy. Autophagy 15, 1677–1681.

Derubeis AR, Young MF, Jia L, Robey PG, Fisher LW (2000). Double FYVE-containing protein 1 (DFCP1): isolation, cloning and characterization of a novel FYVE finger protein from a human bone marrow cDNA library. Gene 255, 195–203.

Dowdle WE, Nyfeler B, Nagel J, Elling RA, Liu S, Triantafellow E, Menon S, Wang Z, Honda A, Pardee G, *et al.* (2014). Selective VPS34 inhibitor blocks autophagy and uncovers a role for NCOA4 in ferritin degradation and iron homeostasis in vivo. Nat Cell Biol 16, 1069–1079.

Ferro-Novick S, Reggiori F, Brodsky JL (2021). ER-phagy, ER homeostasis, and ER quality control: implications for disease. Trends Biochem Sci 46, 630–639.

Forrester A, De Leonibus C, Grumati P, Fasana E, Piemontese M, Staiano L, Fregno I, Raimondi A, Marazza A, Bruno G, *et al*. (2019). A selective ER-phagy exerts procollagen quality control via a calnexin-FAM134B complex. EMBO J 38, e99847.

Fregno I, Fasana E, Bergmann TJ, Raimondi A, Loi M, Solda T, Galli C, D'Antuono R, Morone D, Danieli A, *et al*. (2018). ER-to-lysosome-associated degradation of proteasome-resistant ATZ polymers occurs via receptor-mediated vesicular transport. EMBO J 37, e99259.

Fregno I, Molinari M (2019). Proteasomal and lysosomal clearance of faulty secretory proteins: ER-associated degradation (ERAD) and ER-to-lysosome-associated degradation (ERLAD) pathways. Crit Rev Biochem Mol Biol 54, 153–163.

Fujita E, Kouroku Y, Isoai A, Kumagai H, Misutani A, Matsuda C, Hayashi YK, Momoi T (2007). Two endoplasmic reticulum-associated degradation (ERAD) systems for the novel variant of the mutant dysferlin: ubiquitin/proteasome ERAD(I) and autophagy/lysosome ERAD(II). Hum Mol Genet 16, 618–629.

Grove DE, Fan CY, Ren HY, Cyr DM (2011). The endoplasmic reticulum-associated Hsp40 DNAJB12 and Hsc70 cooperate to facilitate RMA1 E3-dependent degradation of nascent CFTRDeltaF508. Mol Biol Cell 22, 301–314.

Grunwald DS, Otto NM, Park JM, Song D, Kim DH (2020). GABARAPs and LC3s have opposite roles in regulating ULK1 for autophagy induction. Autophagy 16, 600–614.

Hayashi-Nishino M, Fujita N, Noda T, Yamaguchi A, Yoshimori T, Yamamoto A (2009). A subdomain of the endoplasmic reticulum forms a cradle for autophagosome formation. Nat Cell Biol 11, 1433–1437.

Hayashi-Nishino M, Fujita N, Noda T, Yamaguchi A, Yoshimori T, Yamamoto A (2010). Electron tomography reveals the endoplasmic reticulum as a membrane source for autophagosome formation. Autophagy 6, 301–303.

He L, Kennedy AS, Houck S, Aleksandrov A, Quinney NL, Cyr-Scully A, Cholon DM, Gentzsch M, Randell SH, Ren HY, Cyr DM (2021). DNAJB12 and Hsp70 triage arrested intermediates of N1303K-CFTR for ER associated-autophagy. Mol Biol Cell 32, 538–553.

Hipp MS, Kasturi P, Hartl FU (2019). The proteostasis network and its decline in ageing. Nat Rev Mol Cell Biol 20, 421–435.

Houck SA, Ren HY, Madden VJ, Bonner JN, Conlin MP, Janovick JA, Conn PM, Cyr DM (2014). Quality control autophagy degrades soluble ERAD-resistant conformers of the misfolded membrane protein GnRHR. Mol Cell 54, 166–179.

Jastrzebska B, Fotiadis D, Jang GF, Stenkamp RE, Engel A, Palczewski K (2006). Functional and structural characterization of rhodopsin oligomers. J Biol Chem 281, 11917–11922.

Joachim J, Tooze SA (2016). GABARAP activates ULK1 and traffics from the centrosome dependent on Golgi partners WAC and GOLGA2/GM130. Autophagy 12, 892–893.

Joo JH, Dorsey FC, Joshi A, Hennessy-Walters KM, Rose KL, McCastlain K, Zhang J, Iyengar R, Jung CH, Suen DF, *et al*. (2011). Hsp90-Cdc37 chaperone complex regulates Ulk1- and Atg13-mediated mitophagy. Mol Cell 43, 572–585.

Klionsky DJ, Abdel-Aziz AK, Abdelfatah S, Abdellatif M, Abdoli A, Abel S, Abeliovich H, Abildgaard MH, Abudu YP, Acevedo-Arozena A, *et al*. (2021). Guidelines for the use and interpretation of assays for monitoring autophagy (4th edition). Autophagy 17, 1–382.

Ktistakis NT, Tooze SA (2016). Digesting the expanding mechanisms of autophagy. Trends Cell Biol 26, 624–635.

Li K, Jiang Q, Bai X, Yang YF, Ruan MY, Cai SQ (2017). Tetrameric assembly of K(+) channels requires ER-located chaperone proteins. Mol Cell 65, 52–65.

Llambi F, Wang YM, Victor B, Yang M, Schneider DM, Gingras S, Parsons MJ, Zheng JH, Brown SA, Pelletier S, *et al*. (2016). BOK is a non-canonical BCL-2 family effector of apoptosis regulated by ER-associated degradation. Cell 165, 421–433.

Loi M, Molinari M (2020). Mechanistic insights in recov-ER-phagy: micro-ER-phagy to recover from stress. Autophagy 16, 385–386.

McQuin C, Goodman A, Chernyshev V, Kamentsky L, Cimini BA, Karhohs KW, Doan M, Ding L, Rafelski SM, Thirstrup D, *et al*. (2018). CellProfiler 3.0: next-generation image processing for biology. PLoS Biol 16, e2005970.

Meng D, Ragi SD, Tsang SH (2020). Therapy in rhodopsin-mediated autosomal dominant retinitis pigmentosa. Mol Ther 28, 2139–2149.

Papadopoulos C, Meyer H (2017). Detection and clearance of damaged lysosomes by the endo-lysosomal damage response and lysophagy. Curr Biol 27, R1330–R1341.

Park PS (2019). Rhodopsin oligomerization and aggregation. J Membr Biol 252, 413–423.

Pedersen NM, Wenzel EM, Wang L, Antoine S, Chavrier P, Stenmark H, Raiborg C (2020). Protrudin-mediated ER-endosome contact sites promote MT1-MMP exocytosis and cell invasion. J Cell Biol 219, e202003063.

Petherick KJ, Conway OJ, Mpamhanga C, Osborne SA, Kamal A, Saxty B, Ganley IG (2015). Pharmacological inhibition of ULK1 kinase blocks mammalian target of rapamycin (mTOR)-dependent autophagy. J Biol Chem 290, 28726.

Phillips BP, Miller EA (2021). Membrane protein folding and quality control. Curr Opin Struct Biol 69, 50–54.

Proikas-Cezanne T, Pfisterer SG (2009). Assessing mammalian autophagy by WIPI-1/Atg18 puncta formation. Methods Enzymol 452, 247–260.

Proikas-Cezanne T, Ruckerbauer S, Stierhof YD, Berg C, Nordheim A (2007). Human WIPI-1 puncta-formation: a novel assay to assess mammalian autophagy. FEBS Lett 581, 3396–3404.

Proikas-Cezanne T, Takacs Z, Donnes P, Kohlbacher O (2015). WIPI proteins: essential PtdIns3P effectors at the nascent autophagosome. J Cell Sci 128, 207–217.

Proikas-Cezanne T, Waddell S, Gaugel A, Frickey T, Lupas A, Nordheim A (2004). WIPI-1alpha (WIPI49), a member of the novel 7-bladed WIPI protein family, is aberrantly expressed in human cancer and is linked to starvation-induced autophagy. Oncogene 23, 9314–9325.

Pu J, Guardia CM, Keren-Kaplan T, Bonifacino JS (2016). Mechanisms and functions of lysosome positioning. J Cell Sci 129, 4329–4339.

Radulovic M, Schink KO, Wenzel EM, Nahse V, Bongiovanni A, Lafont F, Stenmark H (2018). ESCRT-mediated lysosome repair precedes lysophagy and promotes cell survival. EMBO J 37, e99753.

Ravenhill BJ, Boyle KB, von Muhlinen N, Ellison CJ, Masson GR, Otten EG, Foeglein A, Williams R, Randow F (2019). The cargo receptor NDP52 initiates selective autophagy by recruiting the ULK complex to cytosol-invading bacteria. Mol Cell 74, 320–329.e326.

Saliba RS, Munro PM, Luthert PJ, Cheetham ME (2002). The cellular fate of mutant rhodopsin: quality control, degradation and aggresome formation. J Cell Sci 115, 2907–2918.

Schindelin J, Arganda-Carreras I, Frise E, Kaynig V, Longair M, Pietzsch T, Preibisch S, Rueden C, Saalfeld S, Schmid B, *et al*. (2012). Fiji: an open-source platform for biological-image analysis. Nat Methods 9, 676–682.

Sopha P, Kadokura H, Yamamoto YH, Takeuchi M, Saito M, Tsuru A, Kohno K (2012). A novel mammalian ER-located J-protein, DNAJB14, can accelerate ERAD of misfolded membrane proteins. Cell Struct Funct 37, 177–187.

Sopha P, Ren HY, Grove DE, Cyr DM (2017). Endoplasmic reticulum stress-induced degradation of DNAJB12 stimulates BOK accumulation and primes cancer cells for apoptosis. J Biol Chem 292, 11792–11803.

Thurston TL, Boyle KB, Allen M, Ravenhill BJ, Karpiyevich M, Bloor S, Kaul A, Noad J, Foeglein A, Matthews SA, *et al*. (2016). Recruitment of TBK1 to cytosol-invading Salmonella induces WIPI2-dependent antibacterial autophagy. EMBO J 35, 1779–1792.

Tooze SA, Yoshimori T (2010). The origin of the autophagosomal membrane. Nat Cell Biol 12, 831–835.

Vaites LP, Paulo JA, Huttlin EL, Harper JW (2018). Systematic analysis of human cells lacking ATG8 proteins uncovers roles for GABARAPs and the CCZ1/MON1 regulator C18orf8/RMC1 in macroautophagic and selective autophagic flux. Mol Cell Biol 38, e00392-17.

Vargas JNS, Wang C, Bunker E, Hao L, Maric D, Schiavo G, Randow F, Youle RJ. (2019). Spatiotemporal control of ULK1 activation by NDP52 and TBK1 during selective autophagy. Mol Cell 74, 347–362.e346.

Walczak CP, Ravindran MS, Inoue T, Tsai B (2014). A cytosolic chaperone complexes with dynamic membrane J-proteins and mobilizes a nonenveloped virus out of the endoplasmic reticulum. PLoS Pathog 10, e1004007.

Wilkinson S (2019). Picky eating at the ER-phagy buffet. Trends Biochem Sci 44, 731–733.

Wilkinson S (2020). Emerging principles of selective ER autophagy. J Mol Biol 432, 185–205.

Wirth M, Zhang W, Razi M, Nyoni L, Joshi D, O'Reilly N, Johansen T, Tooze SA, Mouilleron S (2019). Molecular determinants regulating selective binding of autophagy adapters and receptors to ATG8 proteins. Nat Commun 10, 2055.

Yamamoto YH, Kimura T, Momohara S, Takeuchi M, Tani T, Kimata Y, Kadokura H, Kohno K (2010). A novel ER J-protein DNAJB12 accelerates ER-associated degradation of membrane proteins including CFTR. Cell Struct Funct 35, 107–116.

Yla-Anttila P, Vihinen H, Jokitalo E, Eskelinen EL (2009). 3D tomography reveals connections between the phagophore and endoplasmic reticulum. Autophagy 5, 1180–1185.